Predictability of tropical cyclone intensity: scale-dependent forecast error growth in high-resolution stochastic kinetic-energy backscatter ensembles

Falko Judt,[a]* Shuyi S. Chen[a] and Judith Berner[b]

[a]*Rosenstiel School of Marine and Atmospheric Science, University of Miami, FL, USA*
[b]*National Center for Atmospheric Research, Boulder, CO, USA*

Correspondence to: F. Judt, Rosenstiel School of Marine and Atmospheric Science, University of Miami, 4600 Rickenbacker Causeway, Miami, Fl 33149, USA. E-mail: fjudt@rsmas.miami.edu

A systematic study of the intrinsic predictability of tropical cyclone (TC) intensity is conducted using a set of cloud-resolving model ensembles of Hurricane *Earl* (2010). The ensembles are perturbed with a stochastic kinetic-energy backscatter scheme (SKEBS) and started from identical initial conditions. Scale-dependent error growth is investigated by imposing stochastic perturbations with various spatial scales on the TC and its environment. Predictability limits (upper bound) are determined by computing the error magnitude associated with each component of the Fourier-decomposed TC wind fields at forecast times up to 7 days. Three SKEBS ensembles with different perturbation scales are used to investigate the effects of small-scale, mesoscale and large-scale uncertainties on the predictability of TC intensity. In addition, the influence of the environmental flow is investigated by perturbing the lateral boundary conditions. It is found that forecast errors grow rapidly on small scales (azimuthal wave numbers > 20), which saturate within 6−12 h in all four ensembles, regardless of perturbation scale. Errors grow relatively slower on scales corresponding to rain bands (wave numbers 2−5), limiting the predictability of these features to 1−5 days. *Earl*'s mean vortex and the wave number-1 asymmetry are comparatively resistant to error growth and remain predictable for at least 7 days. Forecast uncertainty of the mean vortex and wave number-1 asymmetry is greater in the large-scale perturbation and perturbed lateral boundary condition ensembles. The results from this case indicate that the predictability of the mean vortex and wave number-1 asymmetry is predominately associated with the predictability of the large-scale environment, which is generally much longer than that of convective-scale processes within the TC.

Key Words: tropical cyclones; hurricanes; predictability; ensembles; intensity; error growth

Received 7 October 2014; Revised 23 June 2015; Accepted 1 July 2015; Published online in Wiley Online Library 8 September 2015

1.   Introduction

Predicting tropical cyclone (TC) intensity remains a major challenge in spite of efforts and recent advancements in theory, numerical weather prediction (NWP) and data assimilation (e.g. Rappaport *et al.*, 2009; Gall *et al.*, 2013). As demonstrated by the latest National Hurricane Center (NHC) verification report, the long-term trends of forecast intensity error and forecast skill have improved only a little over the past few years (Cangialosi and Franklin, 2014). The lack of significant improvement and continued struggle to predict TC intensity provokes fundamental questions about the intrinsic predictability of TCs. While there have been extensive studies of the physical processes related to TC intensity uncertainty and predictability, the answer to the question of what is the upper limit of TC intensity predictability remains unknown. To assess the intrinsic predictability of

long-lasting TCs over the open ocean, a comprehensive study of the predictability of TCs within the context of their large-scale environment is needed. Here we begin with a brief review of atmospheric predictability and its applications in TCs.

1.1.   Limited predictability of atmospheric flow

The concept of limited predictability has been established in the atmospheric sciences since Edward Lorenz's ground-breaking work in the 1960s. Following an earlier study on atmospheric predictability by Thompson (1957), Lorenz (1969, hereafter L69) used a relatively simple mathematical model to quantify the scale-dependent growth of errors. He found that multiscale turbulent fluid systems characterized by a '−5/3' power spectrum possess an absolute finite-time predictability barrier due to the rapid upscale growth of small-scale errors. This result was later replicated in

similar experiments using more sophisticated turbulence models (Leith and Kraichnan, 1972; Métais and Lesieur, 1986).

More recently, Rotunno and Snyder (2008, hereafter RS08) extended the original Lorenz model and showed that it is able to reproduce the antithetic predictability characteristics associated with two- and three-dimensional flow regimes: 3-D turbulent flow with a '−5/3' kinetic energy spectrum has *limited* predictability, whereas 2-D flow with a '−3' spectrum possesses *unlimited* predictability (i.e. the predictability can be extended to arbitrarily long time-scales by making the initial error arbitrarily small). This distinction is of particular importance for Earth's atmosphere, since the atmosphere is characterized by a '−3' spectrum at synoptic and larger scales with a transition to a '−5/3' spectrum at the mesoscale (Nastrom and Gage, 1985).

An early mesoscale modelling study by Anthes *et al.* (1985) suggested that the predictability of mesoscale phenomena could exceed that suggested by L69, if they were sufficiently organized/controlled by the large-scale flow. However, the result of Anthes *et al.* (1985) has been unrealistically optimistic given that their experiments were constrained by a relatively small model domain with unperturbed (i.e. 'error free') lateral boundary conditions. Vukicevic and Errico (1990) noted that regional model domains need a critical size (e.g. 4500×4500 km^2) to allow for error growth on synoptic scales.

Other studies have shown that the predictability of mesoscale motions can be severely impacted by error upscaling due to the chaotic behaviour of moist convection (e.g. Zhang *et al.*, 2007). However, although error saturation occurs quickly on convective scales, the results of Zhang *et al.* (2007) also showed that it takes a few days for small-scale errors to substantially influence the predictability of the more slowly evolving synoptic scale.

1.2. Predictability of tropical cyclones

TCs are multiscale in nature. Complex physical processes over a wide range of temporal and spatial scales are known to affect TC structure and intensity, which make it difficult to assess error growth and intrinsic predictability. On one hand, Emanuel *et al.* (2004) and others have emphasized the large-scale environmental control of TC intensity through vertical wind shear (e.g. Black *et al.*, 2002; Chen *et al.*, 2006; Tang and Emanuel, 2012), the upper ocean temperature, and air–sea interactions (Emanuel, 1986; Rotunno and Emanuel, 1987; Chen *et al.*, 2007, 2013; Lin *et al.*, 2013). On the other hand, a number of studies have focused on internal processes and their impact on TC intensity (e.g. Shapiro and Willoughby, 1982; Rozoff *et al.*, 2009; Rogers, 2010). For example, secondary eyewall formation and eyewall replacements are important processes affecting TC intensity. Some studies hypothesized that TC internal processes such as vortex Rossby waves may explain secondary eyewall formation (e.g. Montgomery and Kallenbach, 1997; Wang, 2002). However, using observations from the Hurricane Rainbands and Intensity Experiment (RAINEX) and a high-resolution, full-physics regional model, Judt and Chen (2010) found that inner-core convective processes alone were not able to explain the observed intensity and structure changes in Hurricanes *Katrina* and *Rita* (2005). The question of internal or environmental control of TC intensity remains at the centre of TC predictability.

Studies on predictability of TC intensity have been somewhat limited. TC case-studies that focused on the evolution of forecast uncertainty have used ensemble spread as a proxy for predictability, while other studies relied on idealized models with periodic boundary conditions. Using ensembles with perturbed initial conditions, Sippel and Zhang (2008, 2010) and Zhang and Sippel (2009) assessed the impacts of uncertainties in the atmospheric moisture distribution and the evolution of mesoscale convective systems (MCSs) on TC forecast uncertainty and predictability. They found that TC genesis and subsequent intensification periods are governed by chaotic interactions between MCSs in the pre-genesis stage, and concluded that

the limited predictability of MCSs creates inherent difficulties to accurately predict developing TCs. Hakim (2013) and Brown and Hakim (2013) studied the intrinsic predictability of TC winds using idealized simulations of a mature TC in statistical equilibrium. Results from their idealized simulations indicate that the intrinsic predictability limit of the near-surface winds in TCs is about 2–3 days. However, Brown and Hakim (2013) also pointed out that they were not able to determine the effects of a realistic environment on TC predictability since they used a prescribed, steady environment and periodic boundary conditions. Zhang and Tao (2013) used idealized simulations with a prescribed, variable environment, and found that the TC intensity prediction was strongly influenced by parameters such as vertical wind shear. Tao and Zhang (2014) showed that the uncertainty is due to effects of shear on the intensity and spatial distribution of convection in the intensifying TC. They found substantial uncertainty in the TC evolution, which was heuristically interpreted as a relatively short predictability limit of TC intensity.

Another challenge in TC intensity predictability is the specific metric used to quantify TC intensity. Traditionally, TC intensity is defined as the maximum wind speed at 10 m height anywhere within a TC*. However, the peak surface wind speed at a certain point in time and space does not solely represent the magnitude of the overall circulation, since it is also affected by small-scale turbulent motions within a TC. Vukicevic *et al.* (2014) pointed out that the peak wind metric is not optimal for studying TC intensity and predictability due to the turbulent nature of the TC wind field.

In this study, we assess the intrinsic upper limit of TC intensity predictability using high-resolution cloud-resolving ensemble forecasts. Our predictability approach explicitly takes the multi-scale nature of TC winds into account, and we quantify the scale-dependent error growth in the surface wind field from convective-scale features to the TC vortex scale. Hurricane *Earl* (2010) was chosen for this study because it was an archetypical long-lived Cape-Verde type major hurricane. The model was configured with two vortex-following domains and a large outer domain encompassing most of the western North Atlantic, which enabled the TCs to interact freely with the large-scale environment. The *stochastic kinetic-energy backscatter* (SKEBS: Shutts, 2005; Berner *et al.*, 2009, 2011) algorithm was used to perturb the model ensembles with spatially and temporally correlated patterns of noise.

This article is organized as follows: section 2 contains a description of the ensemble method and error growth analysis technique. Section 3 presents a synopsis of Hurricane *Earl* (2010), and the ensemble predictions of *Earl* are evaluated in section 4. The results of the scale-dependent error growth analysis and predictability analysis are presented in section 5. Section 6 describes the effects of lateral boundary condition perturbations on error growth and TC intensity predictability. The source of predictability is discussed in section 7, and section 8 summarizes the key points of this study.

2. Methodology

2.1. Model set-up

The predictability analysis was performed with output from four different SKEBS ensembles, which were generated with the Weather Research and Forecasting (WRF) – Advanced Research WRF model (WRF-ARW version 3.4, hereafter WRF for simplicity: Skamarock *et al*, 2008). The favourable track record of WRF with regard to TC intensity prediction was documented in Davis *et al.* (2008, 2010).

All ensemble members were initialized with identical analysis fields from the Global Forecasting System (GFS) valid at 0000

---

*The officially assessed 'maximum 1-minute sustained wind speed' is a subjective estimate by NHC forecasters based on available observations. This quantity cannot be measured directly, nor can it be represented by NWP models (Vukicevic *et al.*, 2014).
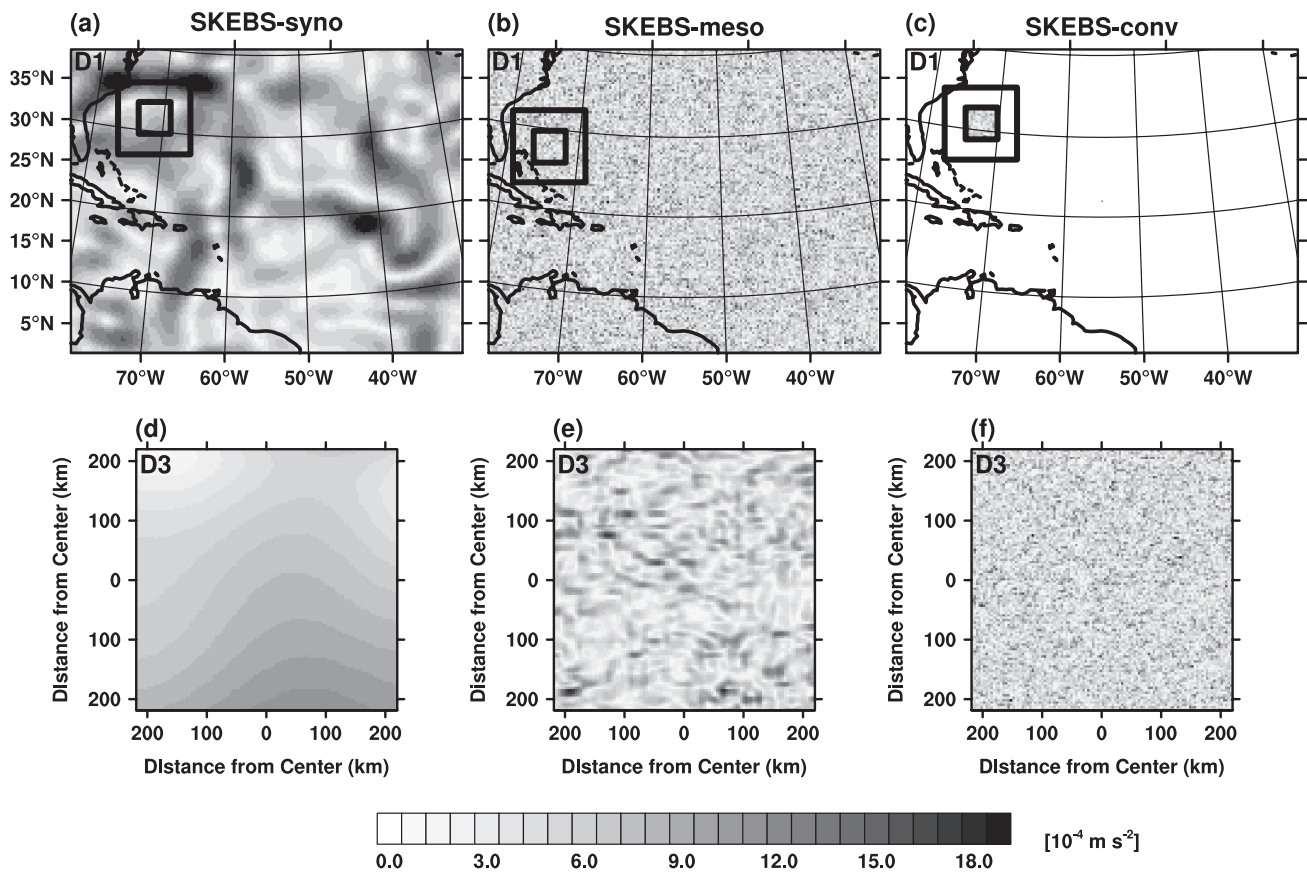
Figure 1. SKEBS wind speed tendency perturbations on the outer model domain from (a) SKEBS-syno, (b) SKEBS-meso and (c) SKEBS-conv. (d)−(f) are the same, but on the innermost moving domain. Moving domains in (a)−(c) are indicated by black rectangles.

UTC on 27 August 2010, when *Earl* was a weak tropical storm with peak winds of $21 \, \text{m s}^{-1}$ (40 kn) while located in the central tropical Atlantic. The ensembles were integrated for 7 days (168 h) using lateral boundary conditions (updated at 6-hourly intervals) from the deterministic 0000 UTC 27 August 2010 GFS forecast. Each member was set up with the stationary outer domain covering most of the western Atlantic and two nested vortex-following grids tracking the TC's centre (the domain set-up is displayed in Figure 1(a−c)). The outer domain had dimensions of 450 × 350 grid points with a grid spacing of $\Delta x_1 = 12$ km, covering an area of 5400 km × 4200 km. These dimensions were large enough to contain the TC during the entire 7-day forecast window and adequate to not overly constrict error growth on synoptic scales (Vukicevic and Errico, 1990). The two vortex-following domains had 250 × 250 and 331 × 331 grid points with grid spacings of $\Delta x_2 = 4$ km and $\Delta x_3 = 1.33$ km, corresponding to areas of 1000 km × 1000 km and 439 km × 439 km, respectively. The dimensions of the innermost domain ensured that the TCs' inner cores and most of their rain bands were inside the domain with $\Delta x_3 = 1.33$ km. There were 44 levels in the vertical, with a relatively higher vertical resolution in the boundary layer. In the outer domain with $\Delta x_1 = 12$ km, convective processes were parametrized with the Kain−Fritsch cumulus scheme while convection was treated explicitly on the two vortex-following grids. The effect of moist physical processes was simulated with the WRF Single-Moment 6-Class Microphysics Scheme (WSM6: Hong and Lim, 2006), planetary boundary-layer processes were parametrized using the Yonsei University scheme (YSU: Hong *et al.*, 2006), and an air−sea flux parametrization based on Donelan *et al.* (2004) and Garratt (1992) was used to account for momentum and enthalpy fluxes at the sea surface (option ISFTCFLX = 2 in the WRF name list).

2.2. The stochastic perturbation method

A stochastic kinetic-energy backscatter scheme (SKEBS: Shutts, 2005; Berner *et al.*, 2009, 2011) was used to add stochastic,

small-amplitude perturbations to the rotational component of the horizontal wind and the potential temperature tendency equations at each time step. The SKEBS technique provides a number of advantages over perturbation techniques that only perturb the initial state. For example, the continuous perturbation of the model fields counteracts the 'error sweeping effect' in regional models with unperturbed boundary conditions (Errico and Baumhefner, 1987). Furthermore, SKEBS provides an elegant and easy way to create scale-dependent perturbations.

For the purpose of the current study, the SKEBS approach can be simply viewed as adding random perturbations with prescribed spatial and temporal decorrelations. A random pattern is created in spectral space with respect to the dimensions of the quadrilateral WRF domain, and each wave number is separately evolved as a first-order autoregressive process. Subsequently, the pattern is transformed back to grid-point space and added to the u, v and θ tendency equations. Temporal correlations are given by the autoregressive parameter, while the perturbation wave-number spectrum determines the spatial correlations. To ensure homogeneity, the *largest* possible perturbation scale is given by the shorter of the two lateral dimensions of the domain (either east−west or north−south). In the experiments described here, the maximum perturbation scale is thus determined by the north−south dimension of the outer domain (i.e. 4200 km). The *smallest* possible perturbation scale is identical to the Nyquist frequency $2^*\Delta x$, where Δx denotes the grid spacing.

As default, the stochastic pattern is generated on the parent domain and interpolated to all nested domains. This limits the smallest perturbation scale on the nested domains to $2^*\Delta x_1 = 24$ km. To perturb smaller scales on the higher-resolved nested domain, the algorithm was changed in order to generate stochastic patterns on each domain independently. With the modified algorithm, it was possible to create SKEBS perturbations as small as $2^*\Delta x_3 = 2.67$ km on the innermost domain.

Table 1. List of SKEBS ensemble experiments.

	SKEBS-syno -PertBdy	SKEBS- syno	SKEBS- meso	SKEBS- conv
Perturbation scale (km)	500–4200	500–4200	24–500	2.67–12
Domains perturbed	1-2-3	1-2-3	1-2-3	3
Perturbed boundaries	Yes	No	No	No

The amplitude of the stochastic perturbations was chosen as the default in WRF. Originally, it was tuned to provide more reliable ensemble spread in the midlatitudes of the WRF mesoscale ensemble (Berner *et al.*, 2011, 2015). Berner *et al.* (2008, 2009) reported that ECMWF predictions in the Tropics were impacted even more favourably than in the midlatitudes, and we assume that the WRF SKEBS perturbations are appropriate for tropical applications. The perturbations used in this study have a random phase vertical structure with westward tilt.

Additionally, we extended the stochastic perturbations to not only perturb the interior of the domain, but also the lateral boundary conditions. Perturbing the lateral boundary conditions simulates uncertainty associated with the flow through the boundaries, which in this case is coming from the deterministic GFS model run. SKEBS boundary condition perturbations are added at every model time step and ease the limitations of a regional model with respect to prescribed forcing through the lateral boundaries.

2.3. Experimental set-up

All experiments were initialized at 0000 UTC 27 August 2010 with the same GFS initial conditions. An unperturbed CNTL forecast and four different SKEBS ensembles were generated to address the question of scale-dependent forecast error growth and the role of lateral boundary condition uncertainty. Each ensemble has 20 members. The spatial scales of the SKEBS perturbations range from synoptic-scale (O(1000 km)) to convective-scale (O(1 km)), spanning a range of 3 orders of magnitude. A listing of the four ensembles with their respective SKEBS characteristics is given in Table 1.

Figure 1 shows a typical example of the SKEBS perturbation patterns. The upper panels display wind speed tendency perturbations on the outer domain, the lower panels zoom in on the innermost grid (the vortex-following domains are indicated by black squares in Figure 1(a–c)). The distinct differences in perturbation scale between SKEBS-syno (Figure 1(a,d)), SKEBS-meso (Figure 1(b,e)) and SKEBS-conv (Figure 1(c,f)) are strikingly evident. Note that SKEBS-conv features perturbations on the innermost domain only. The amplitude of the noise is miniscule, demonstrating that SKEBS perturbations in this set of experiments can be interpreted as 'intrinsic' stochastic noise. Wind speed tendency perturbations do not exceed $1.8 \cdot 10^{-3}$ m s^{-2} (Figure 1), while potential temperature tendency perturbation patterns are on the order of $\pm 10^{-9}$ K s^{-1} (not shown).

2.4. Scale-dependent error growth and predictability limits

Error growth was quantified using the kinetic energy of the 10 m wind. Two metrics are important: the ensemble mean kinetic energy and the ensemble mean error energy, which can be interpreted as a measure of uncertainty. We followed the approach of L69 and RS08, where the predictability limit is defined as the forecast time at which the error saturates.

The hourly model output of the zonal and meridional wind was interpolated to a polar coordinate grid with $r = 0$–300 km, $\mathrm{d}r = 2.0$ km and $\mathrm{d}\theta = 1.0°$ to obtain the surface wind speed field $V(r, \theta)$ of the TCs. At each radius, the V fields were Fourier-decomposed in the azimuthal direction into wave number 0–180 components. For mathematical simplicity, the Fourier

decomposition-based scale analysis only distinguishes scales in the azimuthal direction, and does not take radial variations into account. Despite this simplification, the wave-number fields can be thought of as approximately representing distinct physical structures and different 'scales of motion' in TCs (Figure 2). For example, wave number 0 represents the mean vortex, and wave number 1 the vortex-scale asymmetry. The structure of wave numbers 2–5 resembles TC rain bands, and these components will be referred to as 'rainband-scale'. Azimuthal wave numbers ≥ 6 are associated with smaller mesoscale and convective features in the TC circulation. The relationship between wave numbers in polar coordinates and physical scale is a linear function of radius (for example, an azimuthal wave number-5 feature has a linear scale of 378 km at $r = 300$ km, and a linear scale of 188 km at $r = 150$ km). Since the polar grid has a maximum dimension of $r_{\max} = 300$ km, the mean radius of $r = 150$ km is appropriate for approximating the physical scale of azimuthal wave numbers in an average sense. Rainband-scale features are thus roughly representing scales of 200–500 km in physical space, while small-scale circulations (wave numbers > 50) are associated with scales < 20 km.

Scale-dependent predictability limits were determined by computing the ratio of *ensemble mean error kinetic energy* to *ensemble mean kinetic energy* at hourly forecast time intervals. Both quantities are functions of azimuthal wave number k (or 'scale', Figure 2). The kinetic energy per wave number k is given by

$$E(k) = \frac{1}{2} \int_{r=0}^{300\,\mathrm{km}} |\hat{V}(k,r)|^2 r \mathrm{d}r, \tag{1}$$

where $\hat{V}(k, r)$ is the Fourier component of the wind field associated with wave-number component k (here $0 \leq k \leq 180$). The *ensemble mean kinetic energy* $\overline{K}(k)$, or in short the *mean energy,* is then defined as

$$\overline{E}(k) = \frac{1}{20} \sum_{m=1}^{20} K(m,k), \tag{2}$$

where the summation is over all ensemble members m (here $1 \leq m \leq 20$).

The *ensemble mean error kinetic energy* $\overline{E}(k)$, or in short the *error energy*, is a metric that quantifies the uncertainty. $\overline{E}(k)$ is derived from the error fields e, where e is the wind speed difference field between any two ensemble members. According to the combination formula

$$\binom{20}{2} = \frac{20!}{2!(20-2)!} = 190, \tag{3}$$

there are 190 possible combinations between the 20 members and therefore 190 error fields. Each error field e was Fourier-decomposed, yielding the wave-number components of the error fields, $\hat{e}(k)$. The error energy per wave number is then given by

$$E(k) = \frac{1}{2} \int_{r=0}^{300\,\mathrm{km}} |\hat{e}(k,r)|^2 r \mathrm{d}r, \tag{4}$$

similarly to $\overline{K}(k)$, we now define the *ensemble mean error energy* $\overline{E}(k)$ as the average of all error fields E,

$$\overline{E}(k) = \frac{1}{190} \sum_{l=1}^{190} E(l,k). \tag{5}$$

Since the ensemble was started from identical initial conditions, $\overline{E}(k) = 0$ at $t = 0$. For small t, the error between any two members remains small: $\overline{E}(k) << \overline{K}(k)$. By computing the ratio of error energy $\overline{E}(k)$ to energy $\overline{K}(k)$ over time we can assess the growth of
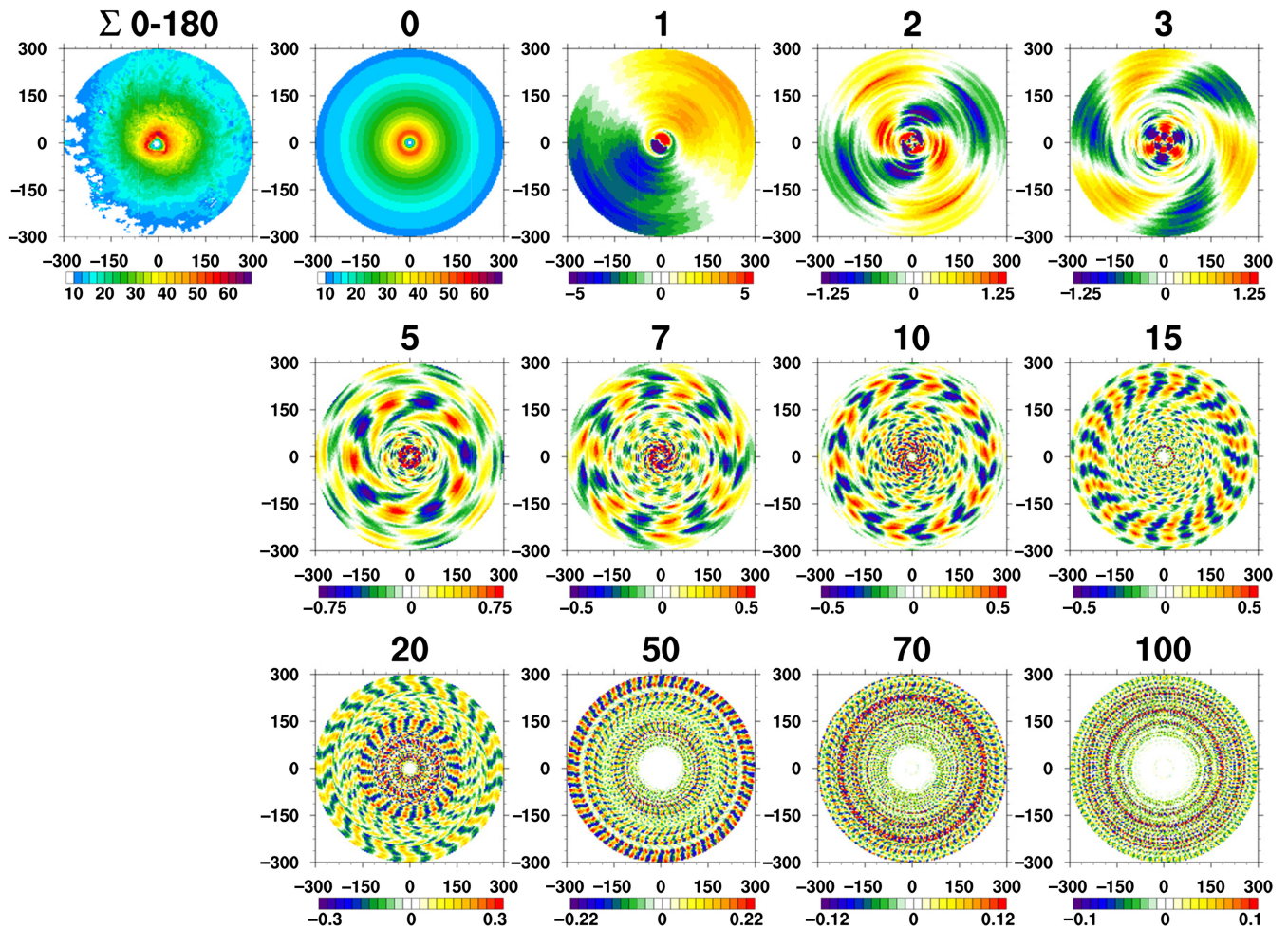
Figure 2. Azimuthal wave number 0, 1, 2, 3, 5, 7, 10, 15, 20, 50, 70, 100 components of the surface wind field. Wave number 0 represents the mean vortex, wave number 1 the vortex scale asymmetry, while wave numbers 2−5 resemble TC rain bands. Higher-order wave numbers are associated with smaller mesoscale and convective-scale elements. The top-left inset is the sum of all wave numbers and equal to the original wind field. Note that the range of the colour bar changes in the various panels.

errors as a function of wave number k. $\overline{E}(k)$ is bounded, and L69 stated that '*if there is no predictability at sufficiently long range,*' $\overline{E} \to 2\overline{K}$. This behaviour is referred to as error saturation, and allows for determining the scale-dependent predictability limit of the Fourier-decomposed TC's wind field. Wave number k loses predictability when

$$\overline{E}(k) = 2 \cdot \overline{K}(k). \qquad (6)$$

The factor 2 in the above equation arises from basic statistics and ensemble theory and can be intuitively explained in the following way: in statistical terms, a forecast is wrong about the correct pattern with variance E. But there will be an additional penalty if a forecast adds an incorrect pattern that also has variance E. The total error would then be $2E$. At this point, the error saturates, cannot grow any further and the total loss of information may be interpreted as a loss of predictability ('the signal gets wiped out by the noise').

It is convenient to substitute, $\overline{E}(k) = 2 \cdot \overline{E^*}(k)$ so that the factor 2 in Eq. (6) disappears. In this case, a loss of predictability of wave number k occurs when the error to energy ratio reaches unity:

$$\frac{\overline{E^*}(k)}{\overline{K}(k)} = 1. \qquad (7)$$

Due to effects of noise and sampling fluctuations, Eqs (6) and (7) are not exact equations, and for practical purposes, we define a loss of predictability when the error ratio reaches 95% of its saturation value (similar to Li and Ding (2011), who used a 90% threshold).

3. Synopsis of Hurricane *Earl* (2010)

Hurricane *Earl* (2010) was a long-lasting tropical cyclone with a typical major hurricane evolution over the Atlantic Ocean, including a period of rapid intensification. It did not make landfall until reaching Nova Scotia, Canada, more than 10 days after its formation, which makes it an ideal candidate for exploring the upper limit of TC predictability.

The cyclone formed from an African Easterly Wave and was declared a tropical depression by NHC at 0600 UTC on 25 August 2010 as it moved westward, steered by the subtropical ridge. *Earl* reached tropical storm strength at 1200 UTC 25 August 2010 and rapidly intensified on 29−30 August to a category-4 hurricane (59 m s^{-1} or 115 kn) while passing north of the Virgin Islands and Puerto Rico. Shortly after, the storm began an eyewall replacement cycle that halted the intensification process. A slight weakening was observed on 1 September, possibly due to an increase in southwesterly shear (Cangialosi, 2010). After the shear abated, the hurricane reintensified while moving northwestward and reached its peak intensity around 0600 UTC on 2 September 2010 with a maximum wind speed of 64 m s^{-1} (125 kn). *Earl* began to turn to the north and started to recurve just south of Cape Hatteras. Weakening commenced as the storm started to interact with the midlatitude flow and began to undergo extratropical transition. *Earl* made landfall on Nova Scotia as a weak hurricane, and was finally designated an extratropical cyclone on 5 September 2010. The time period we chose for this study, 0000 UTC 27 August−0000 UTC 3 September 2010, captures *Earl*'s rapid intensification, its mature stage including the temporary weakening, and the beginning of its extratropical transition phase.
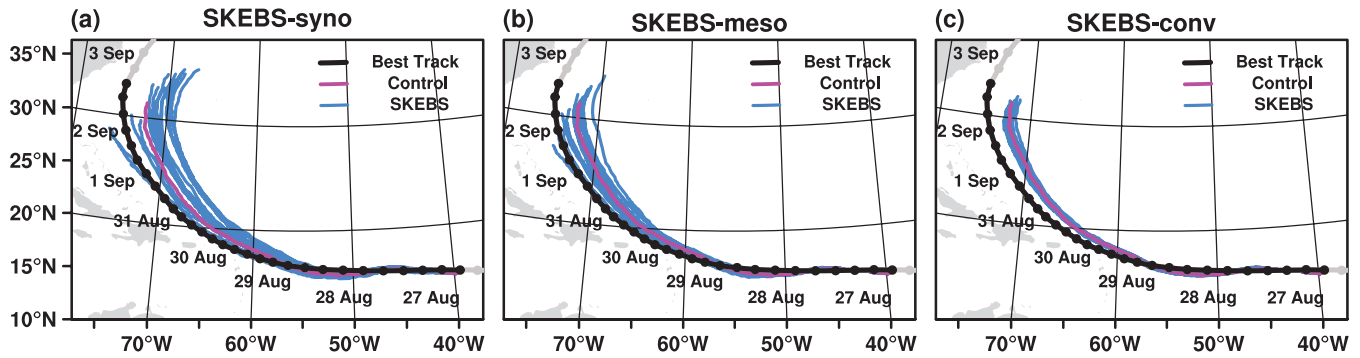
Figure 3. Best-track position estimates (black) and 7-day forecast tracks of Hurricane *Earl* (2010) from (a) SKEBS-syno, (b) SKEBS-meso, and (c) SKEBS-conv ensembles. The control forecast (CTRL) is in magenta.
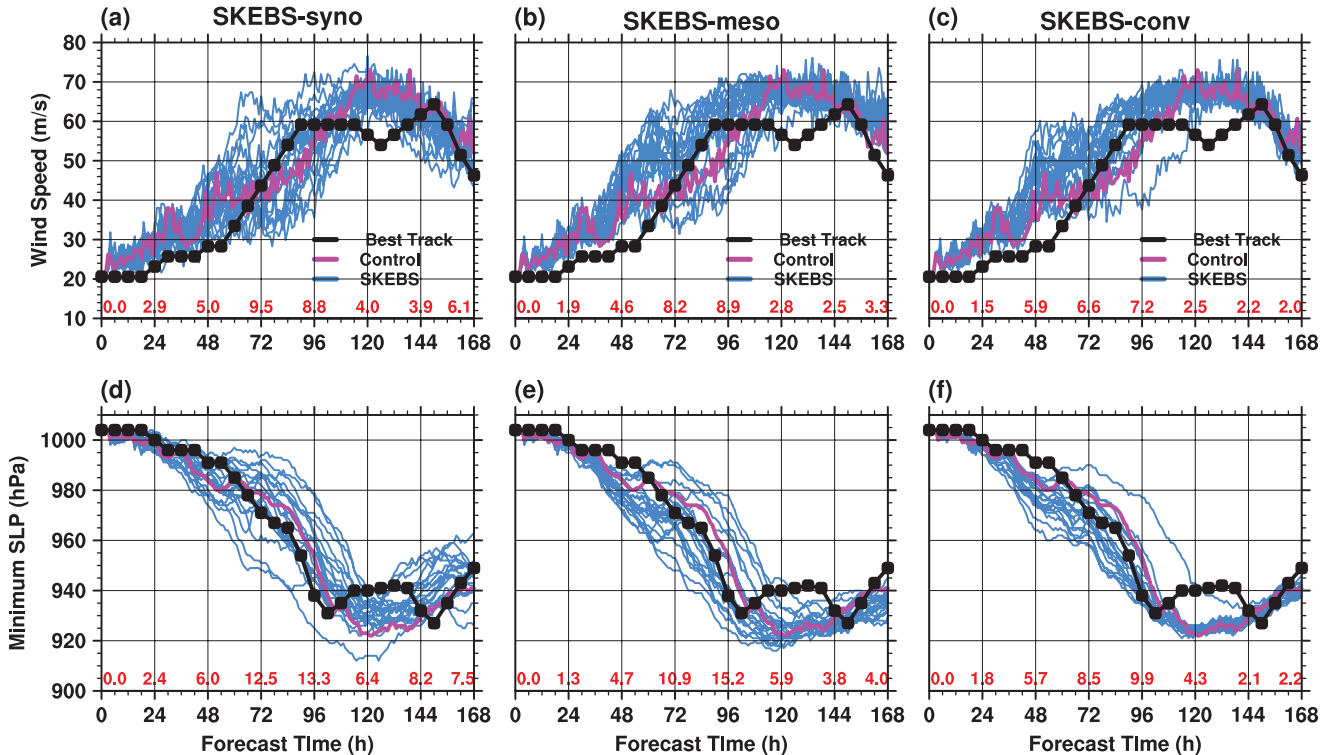

Figure 4. Same as in Figure 3, except for 7-day forecast of (a–c) maximum wind speed and (d–f) minimum sea-level pressure. Ensemble standard deviation values are printed in red above the *x*-axis at 24 h intervals.

4.   Ensemble predictions of Hurricane *Earl*

4.1.   Track uncertainty

Seven-day ensemble track forecasts of *Earl* for the period 0000 UTC 27 August–0000 UTC 3 September 2010 are shown in Figure 3(a) (SKEBS-syno), Figure 3(b) (SKEBS-meso) and Figure 3(c) (SKEBS-conv). The CTRL track (magenta) and *Earl*'s 6-hourly best-track positions are overlaid. Generally, the ensembles correctly predicted *Earl*'s westward motion and its recurvature in the western North Atlantic. A modest eastward bias is noticeable, and the storm's initial turn to the northwest occurs earlier in the forecasts than in reality. Despite this bias, the overall agreement between track forecasts and observations shows that the environmental steering flow was reasonably well captured.

In all three ensembles, track uncertainty increases monotonically with forecast time. Comparing the track uncertainty among the three ensembles reveals that SKEBS-syno exhibits the largest amount of uncertainty (Figure 3(a)), since the synoptic-scale stochastic perturbations project directly onto flow features that control the TC's track. SKEBS-meso exhibits less spread (Figure 3(b)), and the forecast tracks in SKEBS-conv have the least variability (all members are tightly clustered around the CTRL track, Figure 3(c)). The lack of track uncertainty in SKEBS-conv

indicates that perturbing the TC on convective scales does not lead to an effective upscale error growth cascade, and uncertainties in the steering flow during the 7-day forecast period remain minimal.

4.2.   Intensity uncertainty

Maximum wind speed (Figure 4(a–c)) and minimum sea-level pressure forecasts (Figure 4(d–f)) show that the SKEBS ensembles captured the intensity evolution of Hurricane *Earl*, but somewhat overpredicted its intensity. *Earl*'s gradual intensification period (27–29 August 2010, corresponding to forecast time $t = 0–48$ h) was followed by a period of rapid intensification[†], (29–31 August, $t = 48–96$ h), and virtually all ensemble TCs intensified from tropical storms ($v_{max} < 32$ m s^{-1}) to major hurricanes ($v_{max} > 50$ m s^{-1}). After rapid intensification the hurricanes reached a mature state and experienced only minor intensity fluctuations between 31 August and 2 September ($t = 96–144$ h). Subsequently, the TCs weakened as they began extratropical transition (2–3 September, $t = 144–168$ h).

[†]Rapid intensification is commonly defined as an increase in the maximum wind of at least 15.4 m s^{-1} (30 kn) during a 24 h period (Kaplan and DeMaria, 2003).

An intriguing characteristic of the ensembles is that the highest amount of forecast uncertainty is associated with the period of rapid intensification during forecast days 2–4 ($t = 48-96$ h, Figure 4). Nearly all members of the three ensembles undergo rapid intensification, however, at very different timings. In contrast to the monotonically increasing track uncertainty (Figure 3), the intensity uncertainty decreases after $t = 96$ h, indicating that error growth impacts TC intensity differently than TC track. The standard deviations of the ensemble peak wind (σ_w) and sea-level pressure (σ_p) forecasts were calculated at 24 h intervals to provide a more quantitative assessment of uncertainty (red values in Figure 4). In SKEBS-syno (Figure 4(a)), which has the largest intensity spread, the earliest storm starts rapid intensification around $t = 36$ h, while some members do not intensify rapidly until $t = 84$ h. Uncertainty is maximum at $t = 72$ h, when $\sigma_w = 9.5$ m s^{-1}. Figure 4(b) and (c) show a similar behaviour for SKEBS-meso and SKEBS-conv, where the maximum uncertainty also occurs during the rapid intensification period. However, the maximum standard deviations in SKEBS-meso ($\sigma_w = 8.9$ m s^{-1} at $t = 96$ h) and SKEBS-conv ($\sigma_w = 7.2$ m s^{-1} at $t = 96$ h) are smaller compared to SKEBS-syno.

Intensity forecast uncertainty decreases significantly after all storms reach a quasi-steady state with little intensity fluctuations, and σ_w reduces by 60–65% between $t = 72$ and 120 h. None of the members correctly predicted the short period of weakening and reintensification around 1 September 2010 ($t = 120$ h) that was associated with an eyewall replacement cycle and a temporary increase in wind shear. The ensembles did, however, capture *Earl's* weakening as the storm started to lose tropical characteristics, and the intensity forecast uncertainty increases again in SKEBS-syno and SKEBS-meso when the ensemble TCs begin to interact with a midlatitude trough. During the final 24 h, σ_w increases from 3.9 to 6.1 m s^{-1} in SKEBS-syno (Figure 4(a)), and from 2.5 to 3.3 m s^{-1} in SKEBS-meso (Figure 4(b)). The uncertainty evolution in SKEBS-conv is qualitatively different during the final 24 h. The spread continues to shrink between $t = 144-168$ h and σ_w decreases from 2.2 to 2.0 m s^{-1} (Figure 4(c)). Convective-scale perturbations are evidently not able to significantly increase the uncertainty in the large-scale environment, which controls the intensity uncertainty during the extratropical transition period (this result is consistent with the lack of track uncertainty in SKEBS-conv, Figure 3(c)).

The distinct uncertainty differences between the ensembles are more pronounced in the minimum sea-level pressure forecasts (Figure 4(d–f)), which is a more integrated metric of TC intensity. During the rapid intensification period ($t = 48-96$ h), σ_p increases from 6.0 to 13.3 hPa in SKEBS-syno, from 4.7 to 15.2 hPa in SKEBS-meso and from 5.7 to 9.9 hPa in SKEBS-conv. The relative uncertainty minimum after the intensification period is again most distinct in SKEBS-conv. At $t = 168$ h, σ_p collapses to a very small value of 2.2 hPa in SKEBS-conv (Figure 4(f)), while it is twice this value in SKEBS-meso ($\sigma_p = 4.0$ hPa, Figure 4(e)) and almost three times as large in SKEBS-syno ($\sigma_p = 7.5$ hPa, Figure 4(d)).

In summary, all three SKEBS ensembles have significant uncertainty during the rapid intensification period, and minimum uncertainty during peak intensity. SKEBS-conv generally has less uncertainty than the other ensembles. A noteworthy difference between SKEBS-syno and SKESB-conv is the lack of ensemble spread in SKEBS-conv between $t = 144$ and 168 h, indicating reduced uncertainty during extratropical transition.

5. Scale-dependent error growth and its impact on TC predictability

The uncertainty evolution presented in the previous section is a manifestation of error growth in the SKEBS ensembles, and motivates a deeper understanding of how error growth leads to uncertainty and limited predictability. Error growth begins immediately after the first time step. A snapshot of the error
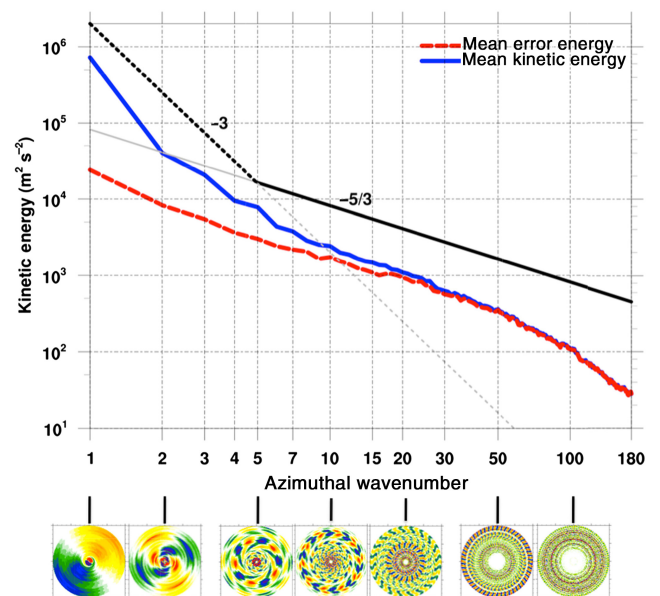

Figure 5. Ensemble mean kinetic energy $\overline{K}(k)$ (blue) and error $\overline{E^*}(k)$ (red) spectra from SKEBS-syno valid at $t = 6$ h. The dashed black line represents a theoretical energy spectrum with a -3 slope, while the solid black line is the same for a $-5/3$ spectrum.

growth process at $t = 6$ h from SKEBS-syno is shown in Figure 5, where error energy $\overline{E^*}(k)$ is in red and mean energy $\overline{K}(k)$ in blue. The wave-number insets below the *x*-axis help to visualize the scales associated with different wave numbers k. Error growth at early times is not entirely consistent with the idealized results from L69 and RS08, and more similar to what Mapes *et al.* (2008) described as 'up-magnitude' growth. From the beginning, errors grow at all scales simultaneously, which is in contrast to L69's original study where the large-scale errors remain zero until the smaller scales saturate. Apparently the SKEBS procedure and error projection from small onto larger scales are growing large-scale errors faster than upscale propagation through successive saturation alone. Despite the error growing on all scales, the error ratio increases more rapidly on smaller scales because of the smaller mean kinetic energy, and saturation occurs after a mere couple of hours. At $t = 6$ h, the error in SKEBS-syno has saturated at all scales corresponding to wave numbers ≥ 30, meaning that features with roughly 30 km spatial scale have lost predictability (Figure 5). The black lines in Figure 5 show theoretical power spectra with slopes of $-5/3$ (solid) and -3 (dashed). Note that the mean energy of the largest scales (wave numbers 1–5) follows a power law with a slope closer to -3, while the spectrum in higher wave numbers behaves more like $-5/3$.

Figure 6 displays $\overline{E^*}(k)$ and $\overline{K}(k)$ at $t = 24$ h from SKEBS-syno (Figure 6(a)), SKEBS-meso (Figure 6(b)) and SKEBS-conv (Figure 6(c)). During the 18 h separating Figures 5 and 6(a), the error in SKEBS-syno has increased at all wave numbers, and the saturation point has spread upscale to wave number 7. SKEBS-meso and SKEBS-conv feature similar error saturation characteristics, but have smaller wave number-1 error magnitudes. By $t = 72$ h, the error has saturated at all scales up to wave number 4 in SKEBS-syno and SKEBS-meso (Figure 7(a,b)), whereas error saturation in SKEBS-conv is only observed up to wave number 7 (Figure 7(c)). The smaller error magnitudes in SKEBS-conv (Figure 7(c)) are consistent with the smaller amount of intensity uncertainty (Figure 4(c,f)). By $t = 120$ h, the mean energy of wave number 0 has increased drastically by almost 100% in all ensembles (Figure 7(d–f)), but the wave number-0 error magnitude has decreased. Since all members have intensified into mature storms by $t = 120$ h (Figure 4), the reduced wave number-0 error is a manifestation of the diminished mean-vortex uncertainty. Towards the end of the forecast, the wave number-0 error increases again due to vortex
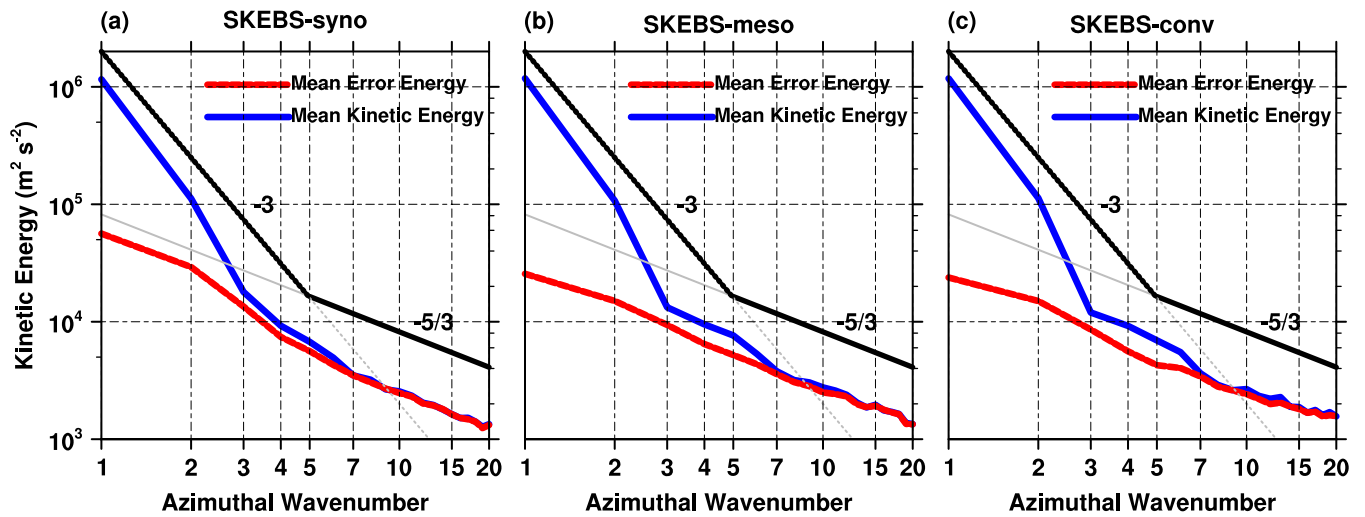
Figure 6. The same as Figure 5, but for (a) SKEBS-syno, (b) SKEBS-meso and (c) SKEBS-conv at forecast hour $t = 24$ h. Only azimuthal wave numbers 1−20 are shown.
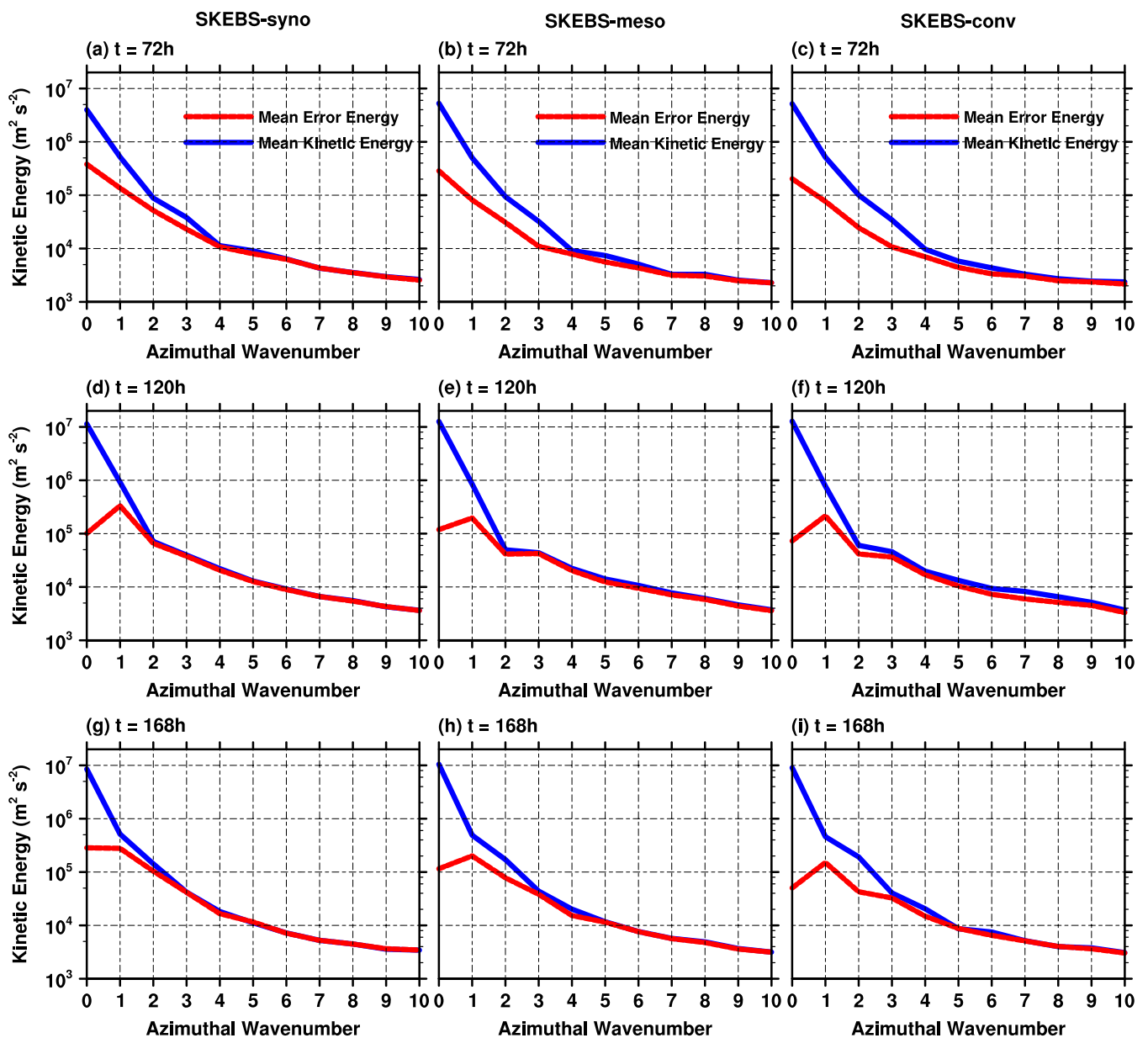

Figure 7. The same as Figure 5, but for (a,d,g) SKEBS-syno, (b,e,h) SKEBS-meso and (c,f,i) SKEBS-conv, valid at forecast hour (a–c) $t = 72$ h, (d–f) $t = 120$ h, and (g–i) $t = 168$ h. The *x*-axis has a linear scale, and only azimuthal wave numbers 0 − 10 are shown.

Table 2. Ratio of error energy $\overline{E^*}$ to mean energy $\overline{K}$ for forecast times $t = 24, 48, 72, 96, 120, 144$ and 168 h and wave numbers $k = 0, 1, 2, 5$ and 10 in SKEBS-syno, SKEBS-meso and SKEBS-conv.

	SKEBS-syno					SKEBS-meso					SKEBS-conv				
	WN0	WN1	WN2	WN5	WN10	WN0	WN1	WN2	WN5	WN10	WN0	WN1	WN2	WN5	WN10
0−24 h	0.01	0.06	0.38	**0.96**	**1.01**	<0.01	0.05	0.26	0.94	**1.01**	<0.01	0.04	0.27	0.91	**0.95**
24−48 h	0.01	0.19	0.93	**1.01**	**1.04**	0.01	0.13	0.92	**0.98**	**1.01**	0.01	0.12	0.79	**0.96**	**1.02**
48−72 h	0.02	0.31	0.81	**0.98**	**1.00**	0.02	0.21	0.71	**1.01**	**1.02**	0.01	0.26	0.65	**0.98**	**1.01**
72−96 h	0.02	0.42	0.88	**1.02**	**1.02**	0.02	0.41	0.83	**1.00**	**1.02**	0.01	0.42	0.88	**0.99**	**1.01**
96−120 h	0.02	0.52	**0.97**	**1.03**	**1.02**	0.01	0.44	0.90	**1.00**	**1.01**	<0.01	0.47	0.84	**0.98**	**1.00**
120−144 h	0.01	0.43	**0.96**	**1.03**	**1.03**	<0.01	0.51	**0.98**	**1.02**	**1.02**	<0.01	0.53	0.91	**1.02**	**1.03**
144−168 h	0.01	0.56	0.82	**1.03**	**1.03**	<0.01	0.51	0.80	**1.03**	**1.02**	<0.01	0.50	0.58	**1.02**	**1.02**

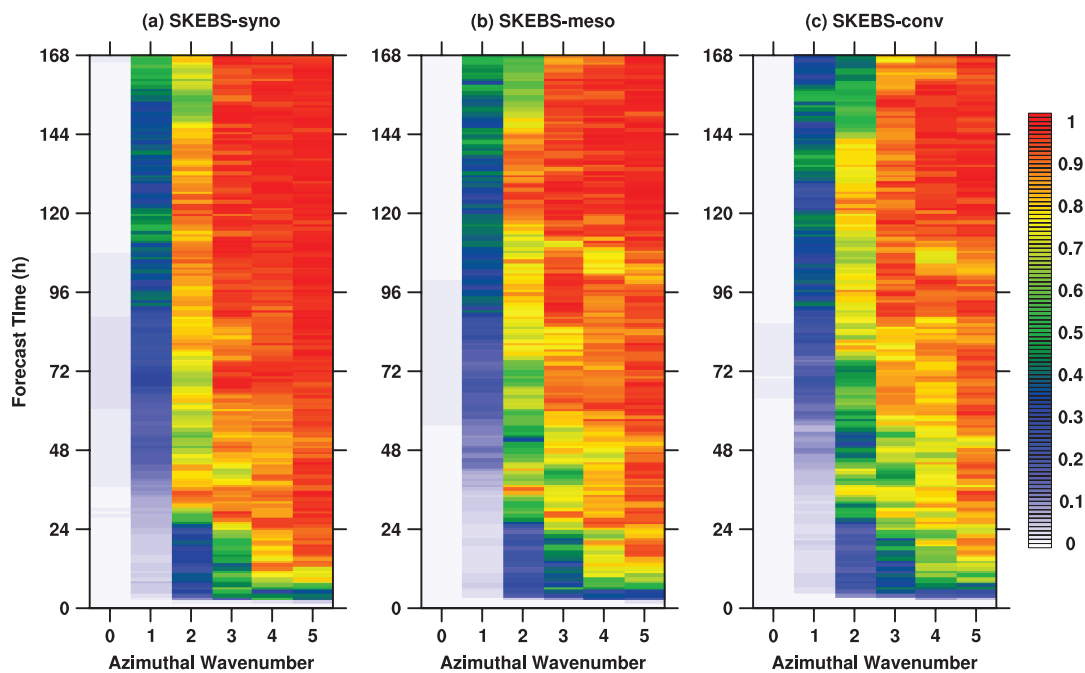When the ratio is ≥0.95 (loss of predictability), values are printed in bold face.

Figure 8. Error to energy ratio (shading) of azimuthal wave numbers 0−5 as a function of forecast time from (a) SKEBS-syno, (b) SKEBS-meso and (c) SKEBS-conv ensembles.

scale uncertainty in response to the beginning of extratropical transition (Figure 7(g−i)). Note that wave numbers 0 and 1 never suffer from error saturation in any of the ensembles throughout the 168 h forecast period (Figure 7(a−i)). This is one of the most remarkable predictability results of this study, and it suggests that the vortex-scale circulation in Hurricane *Earl* has an intrinsic predictability of at least 7 days. It should be noted that maximum wind speed uncertainty may be substantial even if the wave number-0 and 1 wind field components are predictable (Figure 4).

The nature of the logarithmic scale in Figure 7 makes it difficult to directly compare error ratios between the ensembles. A quantitative overview of the error ratio evolution for wave numbers 0, 1, 2, 5 and 10 is shown on Table 2 to better highlight the similarities and differences between the ensembles. Table 2 lists the maximum error ratios occurring within seven 24 h intervals (values are printed in bold face when the value exceeds 0.95). Representative of smaller scales, wave number 10 loses predictability before $t = 24$ h in all ensembles. The wave number-5 error saturates at $t = 17$ h in SKEBS-syno, $t = 29$ h in SKEBS-meso and $t = 35$ h in SKEBS-conv, demonstrating that the wave number-5 predictability is dependent on perturbation scale. Wave number 2 behaves similarly, and error saturation occurs between $t = 96−120$ h in SKEBS-syno and $t = 120−144$ h in SKEBS-meso, but never in SKEBS-conv, implying that wave number-2 rain-band features do not lose predictability in SKEBS-conv.

In contrast to the oscillating wave numbers-2−5 error ratios, which are partly due to differences in mean energy, the wave number-1 error ratio increases more monotonically. In SKEBS-syno, the maximum wave number-1 error ratio (0.56)

occurs late in the forecast between $t = 144−168$ h, and is about 10% larger than the same value in SKEBS-meso and SKEBS-conv. Considering that the wave number-1 asymmetry is a manifestation of shear and/or TC forward motion, a larger wave number-1 error ratio is indicative of increased uncertainty in the environmental flow. This result is consistent with the larger track and intensity uncertainty in SKEBS-syno (Figures 3 and 4), and suggests that the environmental uncertainty is affected more strongly by directly perturbing the large scales (SKEBS-syno) than by upscale error propagation (SKEBS-meso and SKEBS-conv). The error ratio of wave number 0 generally remains very small due to the immense mean energy associated with the well-defined vortex circulations, and never grows beyond 0.02. Nevertheless, the wave number-0 error ratio in SKEBS-syno exceeds that of SKEBS-conv at some forecast times by at least a factor of 2, indicating that the mean vortex circulation in SKEBS-syno has significantly more uncertainty.

Figure 8 gives a visual representation of the error ratio evolution for wave numbers 0−5. SKEBS-syno (Figure 8(a)) features a larger area filled with orange and red colours, indicating higher uncertainty and shorter predictability of wave numbers-2−5 features in comparison with SKEBS-meso (Figure 8(b)) and SKEBS-conv (Figure 8(c)). On scales smaller than wave number 5, error ratios do not show significant differences between the ensembles (not shown). Wave number-0 error ratios remain very small, but their magnitudes increase slightly between $t = 48−72$ h, and feature a relative maximum around $t = 72$ h (Figure 8, Table 2) due to increased vortex-scale uncertainty during the rapid intensification period (Figure 4).
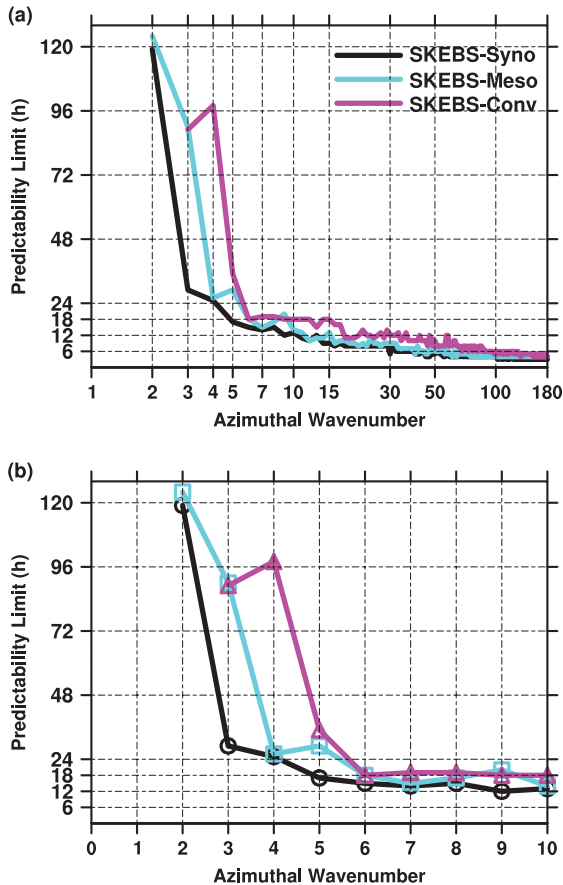
Figure 9. (a) Predictability limits as a function of azimuthal wave number k for SKEBS-syno (black), SKEBS-meso (cyan) and SKEBS-conv (magenta). (b) The same, but on a linear x-scale and only showing wave numbers 0–10. Note that no values are plotted when the predictability limit is >168 h (wave numbers 0 and 1 in SKEBS-syno and SKEBS-meso, wave numbers 0, 1 and 2 in SKBES-conv).

Figure 10. SevendSay forecasts of (a) track, (b) intensity, and (c) minimum sea-level pressure from SKEBS-syno-PertBdy.

In summary, different SKEBS perturbation scales affect the error magnitude on larger TC scales (wave numbers < 5), but do not significantly alter the error growth characteristics at small scales. The results presented in the previous paragraphs can be condensed to (i) bring out the scale-dependency of predictability limits and to (ii) illustrate the relationship between perturbation scales and the predictability of rainband-scale features with wave numbers <5 (Figure 9). In Figure 9, predictability limits are displayed as a function of wave number. All scales associated with wave numbers >7 lose predictability before $t = 24$ h independent of perturbation scale (Figure 9(a)). Figure 9(b) zooms in on wave numbers 0–10. No values are plotted for wave numbers 0 and 1 (SKEBS-syno, SKEBS-meso) and wave numbers 0, 1 and 2 (SKEBS-conv), since these wave numbers never lose predictability. Rainband-scale features have varying predictability limits that clearly depend on perturbation scale. For example, wave number 3 remains predictable for slightly over 24 h in SKEBS-syno, but for almost 96 h in SKEBS-meso and SKEBS-conv. The transitioning from relatively short to long predictability occurs between wave numbers 2 and 5, which approximately corresponds to the scales where the slope of the energy spectrum changes from -3 to $-5/3$. Wave numbers 2 and 5 roughly correspond to physical scales of 500 and 200 km here, consistent with Nastrom and Gage (1985).

6. Effects of lateral boundary condition on TC predictability

A remaining question is whether the predictability of wave numbers 0 and 1 can be attributed to the lack of lateral boundary condition uncertainty, which is a general limitation of regional models (e.g. Errico and Baumhefner, 1987; Vukicevic and Errico, 1990). To investigate the impact of lateral boundary condition uncertainty, the SKEBS-syno-PertBdy ensemble was
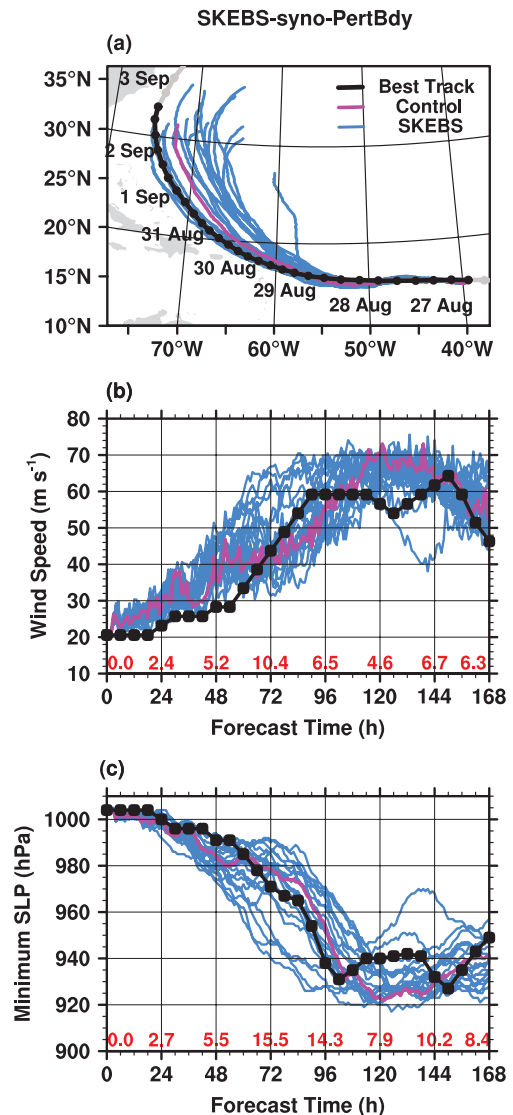
created. In comparison to SKEBS-syno (Figure 3(a)), track uncertainty has increased in SKEBS-syno-PertBdy (Figure 10(a)). Not surprisingly, the SKEBS boundary condition perturbations have evidently increased the variability in the large-scale flow. Intensity uncertainty has also somewhat increased in comparison to SKEBS-syno, likely due to ensemble storms feeling the effects of a more variable environment (Figure 10(b) and (c)).

Figure 11 displays the results of the error growth analysis for forecast hours $t = 72$–168 h. At $t = 72$ h, the error has saturated all scales through to wave number 4 (Figure 11(a)). Two days later, error growth has led to as loss of predictability of wave numbers 2 and 3 (Figure 11(b)), and at the end of the forecast period, only wave numbers 0 and 1 retain predictability (Figure 11(c)). The predictability results from SKEBS-syno-PertBdy are qualitatively comparable to SKEBS-syno, indicating that perturbed lateral boundaries are not able to change the general characteristics of TC intensity predictability in this case. However, the error ratios of wave numbers 0 and 1 in SKEBS-syno-PertBdy are larger than in the SKEBS ensembles without perturbed boundaries. For example, at $t = 168$ h, the wave number-1 error ratio reaches 0.68, which is 20% larger than its respective value in SKEBS-syno (0.56) due to increased variability in the large-scale environment.

7. Source of predictability in TC intensity

In the operational community, TC intensity is defined as the maximum wind speed at 10 m height anywhere within a TC. This
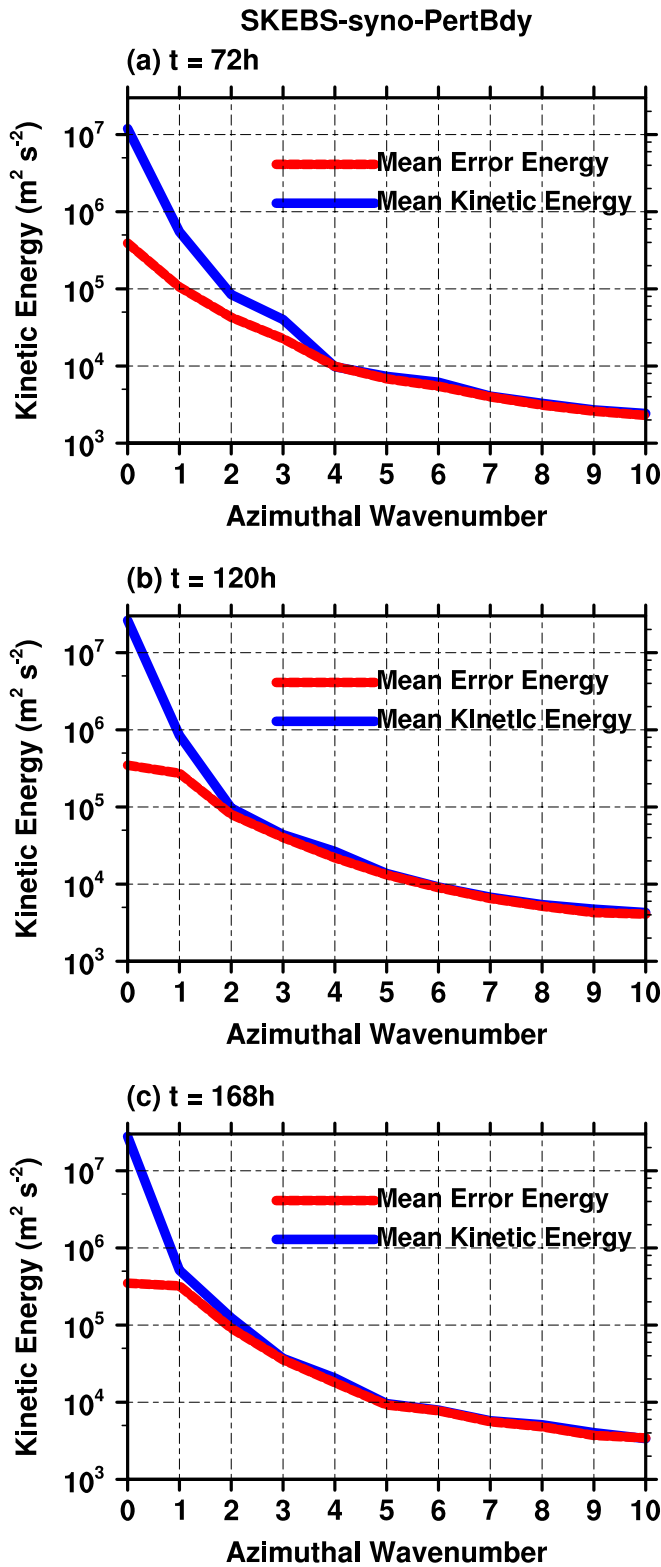
SKEBS-syno-PertBdy

(a) t = 72h

(b) t = 120h

(c) t = 168h

Figure 11. Same as Figure 7, but for SKEBS-syno-PertBdy. (a) $t = 72$ h, (b) $t = 120$ h and (c) $t = 168$ h.

metric has limitations, because it is practically unobservable due to the highly turbulent, rapidly evolving, and spatially extensive wind field in TCs (Vukicevic *et al.*, 2014). By computing a linear fit of the wave numbers-0+1 intensity to the NHC best track intensity data, Vukicevic *et al.* (2014) showed that the circulation represented by wave numbers 0 and 1 contributes roughly 90% to the maximum wind speed in Atlantic hurricanes, while higher-frequency features with shorter predictability limits contribute the remaining 10%. The most critical factor in TC intensity predictability is thus the predictability of the vortex-scale circulation. Sections 5 and 6 demonstrated that the mean vortex and the wave number-1 asymmetry in Hurricane *Earl* were

predictable for at least 7 days. An important question is what leads to the relatively long predictability of these wave-number components. Figure 12 shows the *predictable component* (i.e. the sum of wave numbers 0 and 1) of the 20 TC wind fields from SKEBS-syno at $t = 168$ h. At first glance, all vortices have two basic characteristics in common: a 'doughnut-shape' wind field surrounding a calm centre (the wave number-0 component), and a wave number-1 asymmetry with stronger winds in the eastern semicircles. Predictability of the vortex-scale circulation is a manifestation of these *common* characteristics. However, there are also notable differences between the ensemble members, indicating uncertainty and forecast error. For example, members 1 and 17 (Figure 12(a,q)) resemble mature TCs with strong inner cores and well-defined radii of maximum wind, whereas members 12 and 18 (Figure 12(l, r)) represent TCs in their weakening stage. In the weaker members, the radius of maximum wind is less well defined, the wind field expands, and a stronger wave number-1 asymmetry indicates increasing shear and an increase in translation speed.

The predictable component of the SKEBS-conv vortices (Figure 13) consists of the sum of wave numbers 0−2. A clear northwest-to-southeast oriented wave number-2 feature in the wind fields exhibited by virtually all members is a manifestation of the relative lack of wave number-2 uncertainty in SKEBS-conv. Comparing the pronounced uncertainty in the SKEBS-syno wind fields (Figure 12) with the uniformity in SKEBS-conv (Figure 13) confirms that SKEBS perturbations much smaller than the TC vortex itself translate to significantly less forecast uncertainty on larger scales. The significant differences between Figures 12 and 13 demonstrate that perturbation scale is a key factor in vortex-scale uncertainty. Only perturbations similar in scale to the vortex are able to drastically affect error growth associated with wave numbers 0 and 1. Convective-scale perturbations and error upscaling are not able to impact error growth substantially on the vortex scale, and the vortices look much more similar to each other. Conversely, direct error projection onto larger scales and error downscaling seem to play a much more important role, in agreement with the recent study of Durran and Gingrich (2014). The source of the wave number-0 and 1 predictability is the environment, since the mean vortex is resilient to upscaling convective-scale and mesoscale errors.

One remaining question is how to relate the scale-dependent predictability of the TC wind field to the predictability of the maximum wind speed. By definition, the peak wind is the maximum value of the sum of all wave numbers – some of which may be predictable at a particular time, whereas others may not be. The peak wind is thus composed of a predictable component, and an unpredictable component. A small fraction of the peak wind's predictability is already lost after a few hours due to the short predictability of high wave numbers. However, since the lowest wave numbers remain predictable, a sizable fraction of the maximum wind remains predictable for the entire forecast period. The black shaded area in Figure 14 represents the envelope (i.e. the ensemble range) of the *intensity of the predictable component* (maximum of wave numbers 0+1 in SKEBS-syno, Figure 14(a), and wave numbers 0+1+2 in SKEBS-conv, Figure 14(b)). The maximum wind speed of the sum of the remaining wave-number components is the *intensity of the unpredictable component*, and the overall maximum possible wind speed is the sum of the intensities of the predictable and unpredictable components. This extreme value would only occur if both maxima coincided at the exact location, and represents something like a 'worst case intensity value' (red lines, Figure 14). The black dots in Figure 14 are the actual maximum wind speed values from the ensembles. Note that the predictable component intensity (black shading) is a good approximation of the actual maximum wind speed, in agreement with Vukicevic *et al.* (2014). The difference between the intensity of the predictable component and the actual peak wind is shown as a function of forecast time for SKEBS-syno (Figure 15(a)) and SKEBS-conv (Figure 15(b)). Generally, the differences are $< 6 \, \mathrm{m \, s^{-1}}$
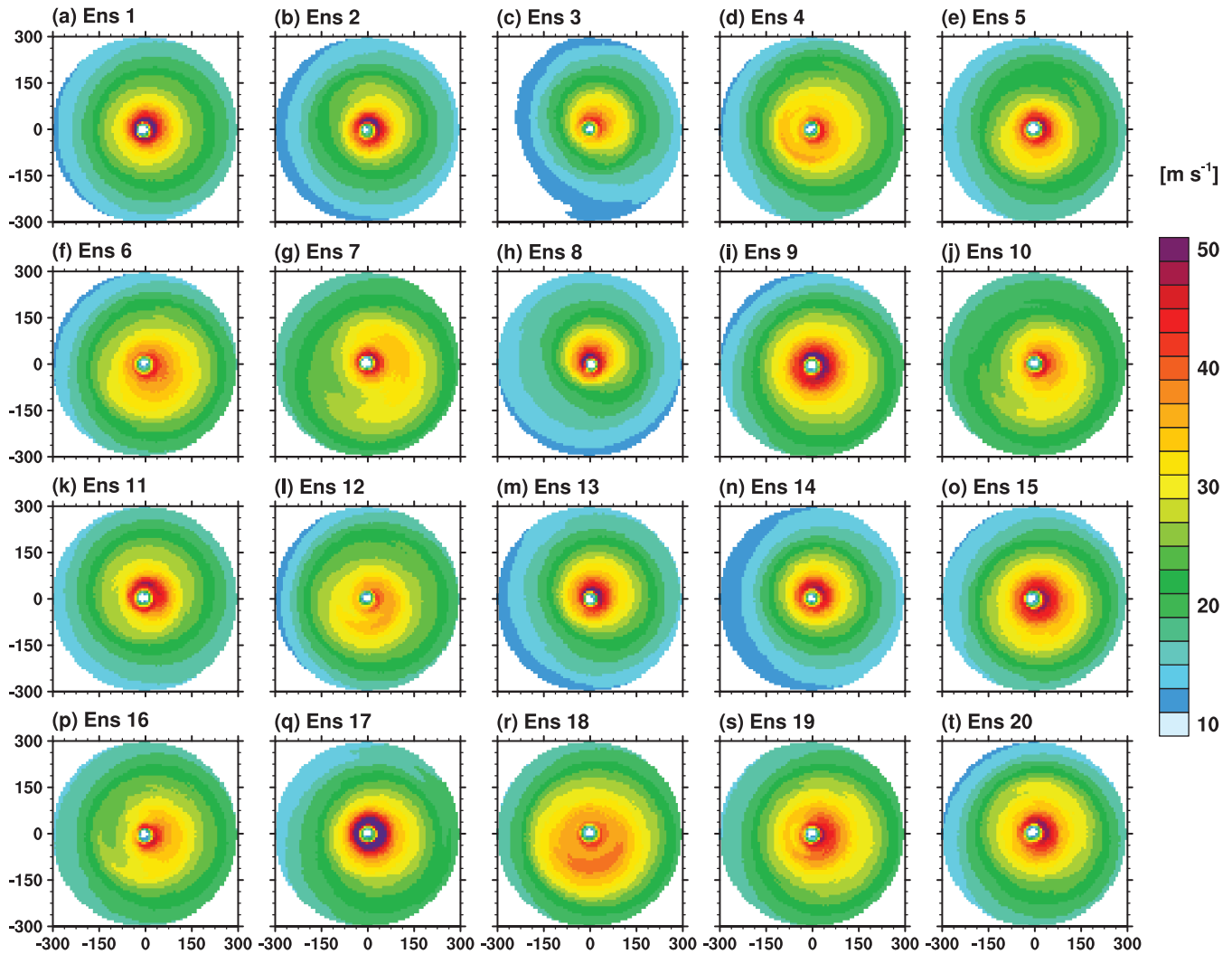
Figure 12. (a)–(t) Sum of the surface wind field's wave number 0 and 1 components from SKEBS-syno at $t = 168$ h.

and there are only very few occasions where the two maxima differ by more than 10 m s^{-1}. Figure 15(c) and (d) show the percentage of the deviation between the predictable component intensity and the peak averaged over the 20 ensemble members. The difference is much less than 10%, supporting the conclusion of Vukicevic *et al.* (2014), who suggested that unpredictable higher wave-number components can be regarded as a stochastic residual.

8. Summary and conclusions

This study explores the upper bound of predictability of TC intensity by investigating scale-dependent error growth in the TC surface wind field. Hurricane *Earl* (2010) is representative of a typical long-lasting major TC over the open ocean. Although the results are based on Hurricane *Earl*, we suspect that they are applicable to TCs with a similar life cycle. We use four high-resolution, cloud-resolving model ensembles perturbed with stochastic perturbations to better understand error growth in the TC surface wind field and its effect on the multiscale nature of TC intensity predictability. The stochastic perturbations have specified spatial and temporal scales that range from convective, to meso-, to synoptic scales (with and without perturbed lateral boundary conditions). This approach allows for (i) quantifying intrinsic, scale-dependent predictability limits in a storm-relative coordinate framework, and (ii) assessing how perturbation scales affect error growth, forecast uncertainty, and the predictability of TC intensity. Scale-dependent predictability limits were determined by computing the error ratios associated with each component of the Fourier-decomposed TC wind fields

at different forecast times. This analysis helps us better understand the multiscale nature of TC winds and potentially identify predictable and unpredictable components that contribute to the maximum wind speed in a TC.

The main results are summarized here:

- It is found that the error grows rapidly and saturates at small scales (wave numbers > 7) within 6–12 h in all four ensembles regardless of perturbation scale (Figures 5 and 6).
- Errors grow relatively slower on scales associated with rain bands (wave numbers 2–5), limiting the predictability of these features to a few days (Figure 7(a–c)).
- The TC mean vortex and asymmetry (wave numbers 0 and 1) are comparatively resistant to upscale error propagation from higher wave numbers and remain predictable for at least 7 days (Figure 7(g–i)).
- Large-scale perturbations and perturbed lateral boundary conditions have larger impacts on TC vortex and forecast uncertainty than perturbations on scales much smaller than the TC vortex (Figures 3, 4, 12 and 13).
- The largest TC intensity forecast uncertainty is found during the rapid intensification in all ensembles (Figures 4 and 14).

The relatively long predictability of the mean TC vortex and wave number-1 asymmetry up to at least 7 days seemingly differs from previous work such as the idealized modelling study by Brown and Hakim (2013), who suggested that TC intensity cannot be predicted beyond 72 h. The main difference of the SKEBS ensemble approach in this study is that it allows for explicit
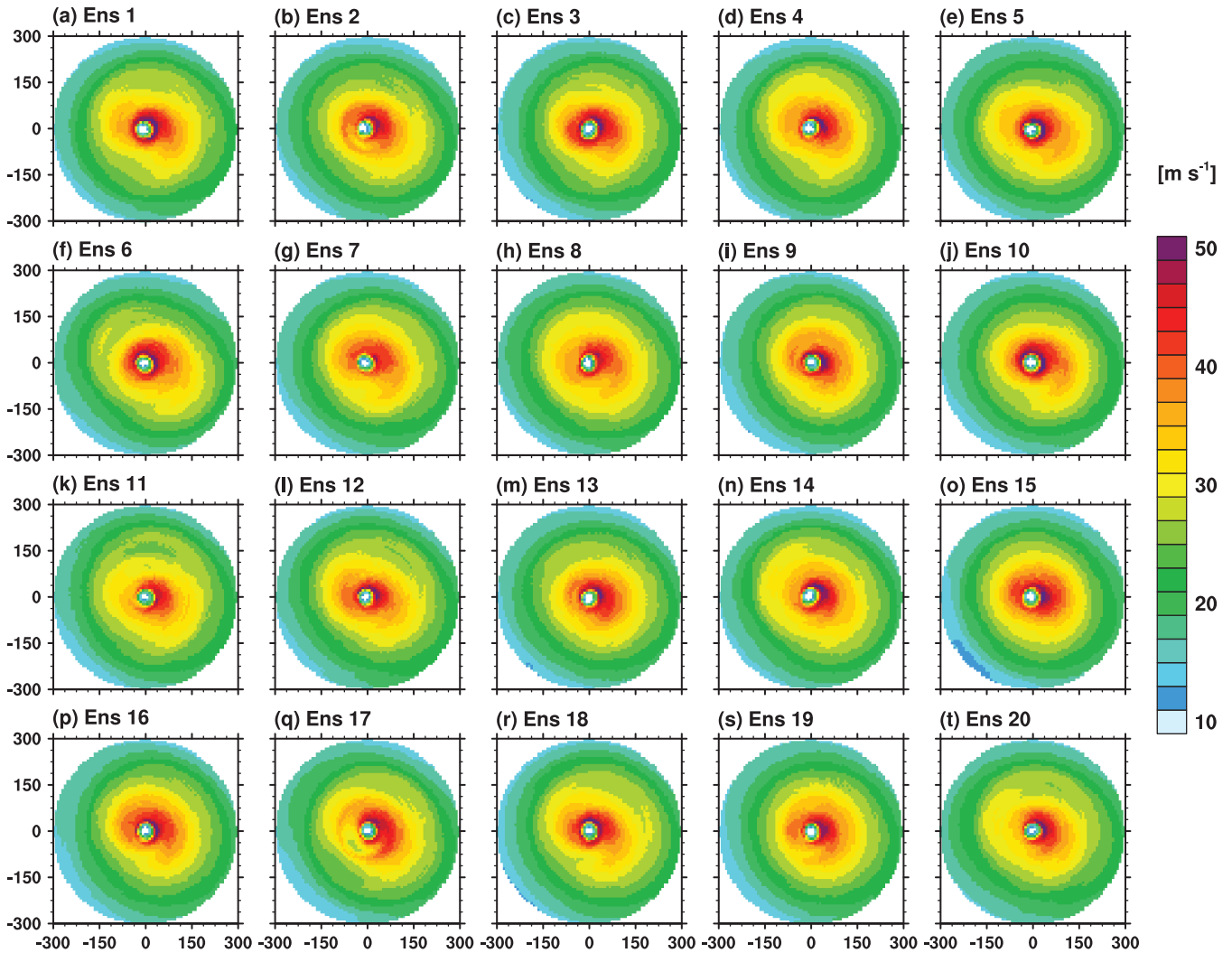
Figure 13. (a)–(t) Same as Figure 12, but from SKEBS-conv and including wave number 2.
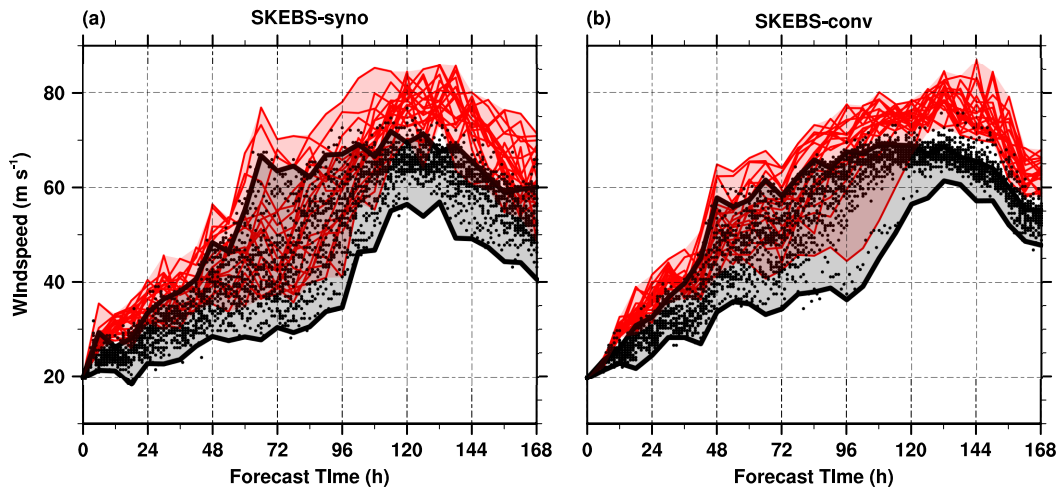

Figure 14. Envelope of the intensity of wave number 0+1 (black shading), the sum of the wave number 0+1 intensity and higher wave-number components (red), and the peak wind speed from each of the ensemble forecasts (black dots) for (a) SKEBS-syno and (b) SKEBS-conv.

TC–environment interactions in a more realistic situation, which seem to be crucial for the relatively longer predictability of the mean TC vortex and wave number-1 asymmetry. This result indicates that the vortex-scale flow is able to inherit the predictability of the large-scale environment of a long-lasting major TC over the open ocean. The relationship can be exemplified by the predictability of wave number-1 asymmetry in a TC, which is mainly a response to environmental wind shear and forward motion of the vortex. The wave number-1 asymmetry should remain predictable as long as the environmental flow responsible for the shear and steering is predictable. The

characteristics of TC wind predictability generally agree with the scale-dependent estimates of L69, and the predictability of the TC vortex and wave number-1 asymmetry is in line with predictability estimates of synoptic-scale flow.

A limitation of the storm-relative analysis is that TC track uncertainty is not explicitly taken into account, although the impact of track variability on TC intensity is reflected by the relatively larger intensity variability in SKEBS-syno and SKEBS-syno-PertBdy. Given that the error growth analysis was performed in a storm-relative coordinate system, the TC intensity predictability limits shown here are therefore storm-relative.
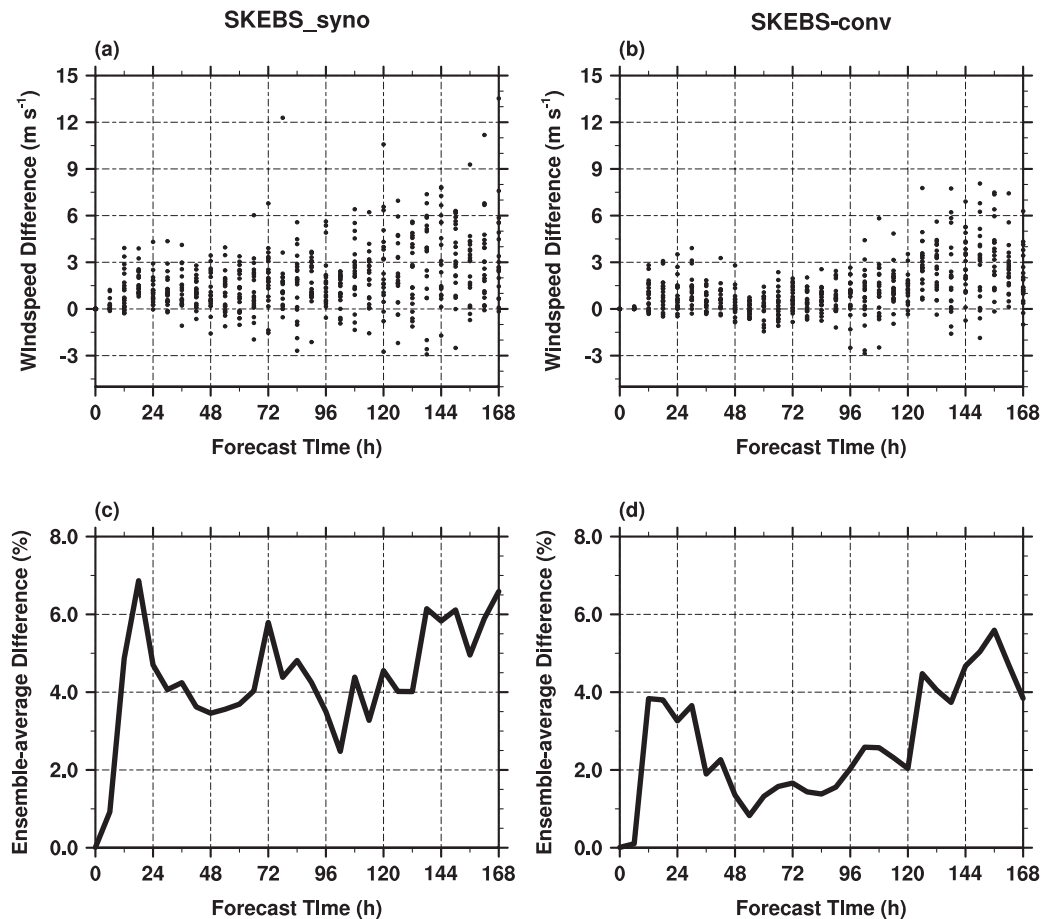
Figure 15. Difference between the peak wind speed and the maximum value of wave numbers 0+1 for (a) SKEBS-syno and (b) SKEBS-conv. Ensemble-average difference between the peak wind speed and the maximum value of wave numbers 0+1 (in per cent) for (c) SKEBS-syno and (d) SKEBS-conv.

They do not represent the predictability of TC-induced winds at a particular geographical location. Another limitation is that we cannot explicitly assess the predictability of certain TC characteristics, such as eyewall replacement cycles, because the error growth associated with these features does not project onto the azimuthal wave-number space.

The error growth is generally characterized by an increase in error magnitude at all scales and not by an upscale cascade as in idealized studies such as L69. Scales associated with wave numbers >5 (less than ∼200 km in spatial scale) have an energy spectrum with a −5/3 slope, and lose predictability in less than a day (Figure 5). However, the larger scales of the TC vortex have an energy spectrum closer to −3 (Figures 6 and 7), indicating that these scales behave more like two-dimensional flow, which in theory has unlimited predictability. We suspect that the barrier resisting upscale error growth is associated with the synoptic-scale environment, which also has an energy spectrum closer to −3. Another possible reason for the relatively long predictability of wave numbers 0 and 1 could be the inertial stability of TC vortices, which tends to suppress error growth on the vortex scale.

The results from this study highlight the importance of the large-scale environment for accurate TC intensity forecasts. In the case of long-lived TCs like Hurricane *Earl*, the environment is able to provide predictability beyond a few days, because it controls the structure and intensity of the mean TC vortex and the wave number-1 asymmetry. However, the importance of the TC's environment comes at a cost. A more uncertain synoptic-scale environment can lead to higher forecast uncertainty of TC intensity and shorter predictability (error downscaling: Durran and Gingrich, 2014). The adverse effect of large wave number-0 and 1 errors on TC intensity predictability has another crucial application. Some artificial vortex-initialization techniques such as 'vortex-bogusing' usually feature an unrealistic vortex structure, which manifests as a large wave number-0 error. To minimize these errors, more advanced initialization techniques

that create a more realistic wave number-0 and 1 structure are essential. Furthermore, in order to decrease the forecast error associated with TC intensity, the uncertainty of the environmental flow needs to be minimized. This study suggests that better observations of the TC environment and the mean TC wind field may lead to more improvement in TC intensity forecasts on synoptic time-scales (5–10 days), compared to increasing observations of the small-scale structure in the TC's inner core.

References

Anthes RA, Kuo Y, Baumhefner DP, Errico RM, Bettge TW. 1985. Prediction of mesoscale atmospheric motions. *Adv. Geophys.* **28B**: 159–202.
Black ML, Gamache JF, Marks FD, Samsury CE, Willoughby HE. 2002. Eastern Pacific hurricanes *Jimena* of 1991 and *Olivia* of 1994: The effect of vertical shear on structure and intensity. *Mon. Weather Rev.* **130**: 2291–2312.
Berner J, Shutts GJ, Leutbecher M, Palmer TN. 2009. A spectral stochastic kinetic energy backscatter scheme and its impact on flow dependent predictability in the ECMWF Ensemble Prediction System. *J. Atmos. Sci.* **66**: 603–626.

Berner J, Ha SY, Hacker JP, Fournier A, Snyder C. 2011. Model uncertainty in a mesoscale ensemble prediction system: Stochastic versus multiphysics representations. *Mon. Weather Rev.* **139**: 1972–1995.

Berner J, Fossell KR, Ha SY, Hacker JP, Snyder C. 2015. Increasing the Skill of Probabilistic Forecasts: Understanding Performance Improvements from Model-Error Representations. *Mon. Wea. Rev.* **143**: 1295–1320, doi: http://dx.doi.org/10.1175/MWR-D-14-00091.1.

Brown BR, Hakim GJ. 2013. Variability and predictability of a three-dimensional hurricane in statistical equilibrium. *J. Atmos. Sci.* **70**: 1806–1820, doi: 10.1175/JAS-D-12-0112.1.

Cangialosi JP. 2010. 'Tropical cyclone report Hurricane Earl'. http://www.nhc.noaa.gov/data/tcr/AL072010_Earl.pdf (accessed 8 June 2015).

Cangialosi JP, Franklin JL. 2014. 'National Hurricane Center forecast verification report'. http://www.nhc.noaa.gov/verification/pdfs/Verification_2013.pdf (accessed 8 June 2015).

Chen SS, Knaff J, Marks FD. 2006. Effect of vertical wind shear and storm motion on tropical cyclone rainfall asymmetry deduced from TRMM. *Mon. Weather Rev.* **134**: 3190–3208.

Chen SS, Price JF, Zhao W, Donelan MA, Walsh EJ. 2007. The CBLAST-Hurricane program and the next-generation fully coupled atmosphere–wave–ocean models for hurricane research and prediction. *Bull. Am. Meteorol. Soc.* **88**: 311–317.

Chen SS, Zhao W, Donelan MA, Tolman HL. 2013. Directional wind–wave coupling in fully coupled atmosphere–wave–ocean models: Results from CBLAST-Hurricane. *J. Atmos. Sci.* **70**: 3198–3215.

Davis C, Wang W, Chen SS, Chen YS, Corboriero K, DeMaria M, Dudhia J, Holland G, Klemp J, Michalakes J, Reeves H, Rotunno R, Snyder C, Xiao QN. 2008. Prediction of landfalling hurricanes with the Advanced Hurricane WRF model. *Mon. Weather Rev.* **136**: 1990–2005, doi: 10.1175/2007MWR2085.1.

Davis C, Wang W, Dudhia J, Torn R. 2010. Does increased horizontal resolution improve hurricane wind forecasts? *Weather and Forecasting* **25**: 1826–1841, doi: 10.1175/2010WAF2222423.1.

Donelan MA, Haus BK, Reul N, Plant WJ, Stiassne M, Graber HC, Brown OB, Saltzman ES. 2004. On the limiting aerodynamic roughness of the ocean in very strong winds. *Geophys. Res. Lett.* **31**: L18306, doi: 10.1029/2004GL019460.

Durran DR, Gingrich M. 2014. Atmospheric predictability: Why butterflies are not of practical importance. *J. Atmos. Sci.* **71**: 2476–2488, doi: 10.1175/JAS-D-14-0007.1.

Emanuel KA. 1986. An air–sea interaction theory for tropical cyclones. Part I: Steady-state maintenance. *J. Atmos. Sci.* **43**: 585–604.

Emanuel KA, DesAutels C, Holloway C, Korty R. 2004. Environmental control of tropical cyclone intensity. *J. Atmos. Sci.* **61**: 843–858, doi: 10.1175/1520-0469(2004)061<0843:ECOTCI>2.0.CO;2.

Errico RM, Baumhefner D. 1987. Predictability experiments using a high-resolution limited-area model. *Mon. Weather Rev.* **115**: 488–504, doi: 10.1175/1520-0493(1987)115<0488:PEUAHR>2.0.CO;2.

Gall R, Franklin JD, Marks FD, Rappaport EN, Toepfer F. 2013. The hurricane forecast improvement project. *Bull. Am. Meteorol. Soc.* **94**: 329–343, doi: 10.1175/BAMS-D-12-00071.1.

Garratt JR. 1992. *The Atmosphere Boundary Layer*. Cambridge University Press: Cambridge, UK.

Hakim GJ. 2013. The variability and predictability of axisymmetric hurricanes in statistical equilibrium. *J. Atmos. Sci.* **70**: 993–1005, doi: 10.1175/JAS-D-12-0188.1.

Hong SY, Lim JOJ. 2006. The WRF single-moment 6-class microphysics scheme (WSM6). *J. Korean Meteorol. Soc.* **42**: 129–151.

Hong SY, Noh Y, Dudhia J. 2006. A new vertical diffusion package with an explicit treatment of entrainment processes. *Mon. Weather Rev.* **134**: 2318–2341, doi: 10.1175/MWR3199.1.

Judt F, Chen SS. 2010. Convectively generated potential vorticity in rainbands and formation of the secondary eyewall in Hurricane *Rita* of 2005. *J. Atmos. Sci.* **67**: 3581–3599, doi: 10.1175/2010JAS3471.1.

Kaplan J, DeMaria M. 2003. Large-scale characteristics of rapidly intensifying tropical cyclones in the North Atlantic Basin. *Weather and Forecasting* **18**: 1093–1108, doi: 10.1175/1520-0434(2003)018<1093:LCORIT>2.0.CO;2.

Leith CE, Kraichnan RH. 1972. Predictability of turbulent flows. *J. Atmos. Sci.* **29**: 1041–1058.

Li J, Ding R. 2011. Temporal–spatial distribution of atmospheric predictability limit by local dynamical analogs. *Mon. Weather Rev.* **139**: 3265–3283, doi: 10.1175/MWR-D-10-05020.1.

Lin I-I, Black P, Price JF, Yang C-Y, Chen SS, Lien C-C, Harr P, Chi N-H, Wu C-C, D'Asaro EA. 2013. An ocean coupling potential intensity index for tropical cyclones. *Geophys. Res. Lett.* **40**: 1878–1882, doi: 10.1002/grl.50091.

Lorenz EN. 1969. The predictability of a flow which possesses many scales of motion. *Tellus* **21**: 289–307.

Mapes BE, Tulich S, Nasuno T, Satoh M. 2008. Predictability aspects of global aqua planet simulations with explicit convection. *J. Meteorol. Soc. Jpn.* **86A**: 175–185.

Métais O, Lesieur M. 1986. Statistical predictability of decaying turbulence. *J. Atmos. Sci.* **43**: 857–870, doi: 10.1175/1520-0469(1986)043,0857: SPODT.2.0.CO;2.

Montgomery MT, Kallenbach RJ. 1997. A theory for vortex Rossby-waves and its application to spiral bands and intensity changes in hurricanes. *Q. J. R. Meteorol. Soc.* **123**: 435–465.

Nastrom GD, Gage KS. 1985. A climatology of atmospheric wavenumber spectra of wind and temperature observed by commercial aircraft. *J. Atmos. Sci.* **42**: 950–960, doi: 10.1175/1520-0469(1985)042<0950: ACOAWS>2.0.CO;2.

Rappaport EN, Franklin JL, Avila LA, Baig SR, Beven JL II, Blake ES, Burr CA, Jiing J, Juckins CA, Knabb RD, Landsea CW, Mainelli M, Mayfield M, McAdie CJ, Pasch RJ, Sisko S, Stewart SR, Tribble AN. 2009. Advances and challenges at the National Hurricane Center. *Weather and Forecasting* **24**: 395–419, doi: 10.1175/2008WAF2222128.1.

Rogers R. 2010. Convective-scale structure and evolution during a high-resolution simulation of tropical cyclone rapid intensification. *J. Atmos. Sci.* **67**: 44–70, doi: 10.1175/2009JAS3122.1.

Rotunno R, Emanuel KA. 1987. An air–sea interaction theory for tropical cyclones. Part II: Evolutionary study using a nonhydrostatic axisymmetric numerical model. *J. Atmos. Sci.* **44**: 542–561.

Rotunno R, Snyder C. 2008. A generalization of Lorenz's model for the predictability of flows with many scales of motion. *J. Atmos. Sci.* **65**: 1063–1076, doi: 10.1175/2007JAS2449.1.

Rozoff CM, Kossin JP, Schubert WH, Mulero PJ. 2009. Internal control of hurricane intensity variability: The dual nature of potential vorticity mixing. *J. Atmos. Sci.* **66**: 133–147, doi: 10.1175/2008JAS2717.1.

Shapiro LJ, Willoughby HE. 1982. The response of balanced hurricanes to local sources of heat and momentum. *J. Atmos. Sci.* **39**: 378–394, doi: 10.1175/1520-0469(1982)039<0378:TROBHT>2.0.CO;2.

Shutts GJ. 2005. A kinetic energy backscatter algorithm for use in ensemble prediction systems. *Q. J. R. Meteorol. Soc.* **131**: 3079–3102.

Sippel JA, Zhang F. 2008. A probabilistic analysis of the dynamics and predictability of tropical cyclogenesis. *J. Atmos. Sci.* **65**: 3440–3459, doi: 10.1175/2008JAS2597.1.

Sippel JA, Zhang F. 2010. Factors affecting the predictability of Hurricane *Humberto* (2007). *J. Atmos. Sci.* **67**: 1759–1778, doi: 10.1175/2010JAS3172.1.

Skamarock WC, Klemp JB, Dudhia J, Gill DO, Barker DM, Duda MG, Huang XY, Wang W, Powers JG. 2008. 'A description of the advanced research WRF version 3', Technical Note TN-475+STR. NCAR: Boulder, CO.

Tang B, Emanuel KA. 2012. Sensitivity of tropical cyclone intensity to ventilation in an axisymmetric model. *J. Atmos. Sci.* **67**: 1817–1830, doi: 10.1175/2010JAS3318.1.

Tao D, Zhang F. 2014. Effect of environmental shear, sea-surface temperature, and ambient moisture on the formation and predictability of tropical cyclones: An ensemble-mean perspective. *J. Adv. Model. Earth Syst.* **6**: 384–404, doi: 10.1002/2014MS000314.

Thompson PD. 1957. Uncertainty of initial state as a factor in the predictability of large scale atmospheric flow patterns. *Tellus* **9**: 275–295.

Vukicevic T, Errico RM. 1990. The influence of artificial and physical factors upon predictability estimates using a complex limited-area model. *Mon. Weather Rev.* **118**: 1460–1482, doi: 10.1175/1520-0493(1990) 118<1460:TIOAAP>2.0.CO;2.

Vukicevic T, Uhlhorn EW, Reasor PD. 2014. A novel multi-scale intensity metric for evaluation of tropical cyclone intensity forecasts. *J. Atmos. Sci.* **71**: 1292–1304, doi: 10.1175/JAS-D-13-0153.1.

Wang Y. 2002. Vortex Rossby waves in a numerically simulated tropical cyclone. Part II: The role in tropical cyclone structure and intensity changes. *J. Atmos. Sci.* **59**: 1239–1262.

Zhang F, Sippel JA. 2009. Effects of moist convection on hurricane predictability. *J. Atmos. Sci.* **66**: 1944–1961, doi: 10.1175/2009JAS2824.1.

Zhang F, Tao D. 2013. Effects of vertical wind shear on the predictability of tropical cyclones. *J. Atmos. Sci.* **70**: 975–983, doi: 10.1175/JAS-D-12-0133.1.

Zhang F, Bei N, Rotunno R, Snyder C, Epifanio CC. 2007. Mesoscale predictability of moist baroclinic waves: Convection-permitting experiments and multistage error growth dynamics. *J. Atmos. Sci.* **64**: 3579–3594, doi: 10.1175/JAS4028.1.